scientific reports

OPEN

Machine learning-optimized compact dual-band medical syringe-inspired wearable antenna for efficient WBAN applications

Muhammad S. Yahya[1], Umar Musa[2], Mohammad S. Zidan[3], Socheatra Soeung[1], Lila Iznita Izhar[1], Z. Zakaria[4] & Ahmed J. A. AL-Gburi[4]✉

This study introduces a compact, machine learning (ML)-enhanced dual-band antenna designed specifically for wearable applications within Wireless Body Area Networks (WBANs). Wearable antennas in WBAN applications face challenges such as human body-induced electromagnetic interference, limited bandwidth, and SAR compliance, which hinder the effective performance of conventional designs. This work addresses these issues by employing machine learning (ML) to optimize the antenna design, thereby ensuring enhanced performance and adaptability in dynamic, on-body environments. The antenna is fabricated on a flexible 30 × 48.8 mm² Rogers Duroid 3003™ substrate, and operates efficiently at 2.4 GHz and 5.8 GHz, achieving fractional bandwidths of 9.7% and 7.8%, peak gains of 4.0 dBi and 6.2 dBi, and high radiation efficiencies of 91% and 93%, respectively. The radiation profile shows a bidirectional pattern along the E-plane, while the H-plane maintains nearly uniform radiation in all directions at both frequency bands. Compliance with safety regulations was confirmed through Specific Absorption Rate (SAR) analysis, with values of 1.17 W/kg (1 g) and 0.851 W/kg (10 g) at 2.4 GHz, and 0.813 W/kg (1 g) and 0.267 W/kg (10 g) at 5.8 GHz, all well below the regulatory thresholds set by FCC and ICNIRP. Mechanical flexibility and robustness were validated through testing under bent conditions on various body regions including the chest, arm, and lap, reflecting reliable operation in realistic WBAN use cases. Additionally, antenna resonant frequency was predicted using a supervised ML regression approach. Among the evaluated algorithms, the random forest model provided the best performance with an R² value of 87.70% and low error metrics (MAE: 0.35, MSE: 0.89, MSLE: 0.21, RMSLE: 0.35, RMSE: 0.94). These results confirm the antenna's reliability, safety, and adaptability for body-worn wireless systems.

Keywords Machine learning, Wearable antenna, Wireless body area network (WBAN), Dual-band, Regression algorithm, Specific absorption rate (SAR), Bending investigation

The field of wearable electronics in wireless WBAN has gained significant interest due to its diverse applications, including fitness tracking, smartwatches, medical care, military systems, and IoT technologies[1,2] as illustrated in Fig. 1. WBAN communication operates through three distinct modes on-body, off-body, and in-body – depending on the spatial arrangement of signal nodes[3,4]. To meet the growing demand for high data rates and reliable connectivity, antennas play a crucial role. However, designing antennas on flexible materials suitable for curved surfaces or direct integration with the human body remains a key challenge for researchers. Wearable antennas offer notable advantages, such as bendability for conformal placement, unobtrusive design, lightweight construction, and low cost, making them ideal for WBAN applications[5–7]. In practice, these antennas are often embedded into clothing or wearable devices, which operate in close proximity to the body. A critical concern is the degradation of antenna performance caused by the human body's electromagnetic interaction. Additionally, minimizing radiation exposure to biological tissues is essential for user safety. Organizations such as the Federal

[1]Department of Electrical and Electronic Engineering, Universiti Teknologi PETRONAS, Seri Iskandar, Perak 32610, Malaysia. [2]Department of Electrical Engineering, Bayero University, Kano 3011Kano PMB, Nigeria. [3]Department of Electrical Techniques, Technical Institute of Anbar, Middle Technical University, Baghdad 10074, Iraq. [4]Center for Telecommunication Research & Innovation (CeTRI), Fakulti Teknologi dan Kejuruteraan Elektronik dan Komputer (FTKEK), Universiti Teknikal Malaysia Melaka (UTeM), Durian Tunggal, Melaka 76100, Malaysia. ✉email: ahmedjamal@al-gburi.org; ahmedjamal@ieee.org

Fig. 1. Recent development and application for wearable electronics[38].

Communications Commission (FCC) in the United States and the European Union (EU) implement specific absorption rate (SAR) regulations to maintain acceptable radiation exposure. According to these guidelines, SAR should not exceed 1.6 W/kg averaged over 1 gram of tissue under FCC rules, and 2 W/kg averaged over 10 g of tissue as per the ICNIRP standards[8].

To address these challenges, numerous antenna designs featuring flexibility and wearability have been proposed for WBAN, including planar monopoles[9,10], dipoles[11,12], slot antennas[13,14], fractal designs[15,16], and microstrip patch antennas[17,18]. A monopole antenna-based multiband fractal antenna with a dendritic topology was introduced[19]. A substrate made of polyimide was utilized during the antenna design process. The SAR number failed to be stated, despite the antenna's ability to perform well. Fractal antennas designed for 2.4 GHz applications, such as the one proposed in[20], achieve compactness but suffer from a narrow fractional bandwidth (FBW) of 7.75%. This limited bandwidth makes the antenna prone to impedance mismatch when exposed to human body-induced detuning. Similarly, the triangular patch antenna in[21] and the CPW-fed slot antenna for ISM bands in[22] exhibit constrained operational bandwidths, with the latter achieving only 6% FBW around 5.83 GHz. Although these designs aim to be compact, they often sacrifice performance, showing the challenge of balancing small size with reliable operation. Miniaturization remains a central challenge in wearable antenna design. Techniques such as resonator elongation[23], quarter-mode structures[24], high-permittivity substrates[25], reactive loading[26], and shorting pins[27] effectively reduce dimensions but often degrade efficiency, restrict bandwidth, or increase fabrication complexity. For example, a metamaterial-based dual-band EBG antenna for wearable applications in[28] mitigates human body interference and SAR using a 2 × 2 EBG reflector, though this approach sacrifices low-profile construction. Textile substrates, favored for their low dielectric constants and reduced surface wave loss, was proposed in[29], but face limitations in SAR compliance. The authors in[30] presents a wearable MIMO UWB antenna with a broad frequency range (1.83–13.82 GHz) and good port isolation, utilizing a jeans cloth substrate. Despite its advantages, the antenna's larger size limits its compactness, making it less suitable for many wearable applications. In a similar vein, a wearable textile antenna with an integrated 90 mm x 60 mm AMC, offering good bandwidth and stability under deformation was presented in[31]. While the antenna performs well, the large volume of antenna may limit its suitability for compact wearable applications. Furthermore, a multiband wearable antenna for WBAN applications, featuring a CPW-fed slot dipole antenna with inductively coupled resonators, was presented in[32]. Though this antenna provides multiband operation and SAR compliance, its larger size (60×40 mm^3) could hinder its use in compact wearable devices. Similarly, a CPW-fed ultrawideband (UWB) antenna for tumor cell detection in the human breast was presented in[33], offering a wide bandwidth (2.26–13.71 GHz) with a fractional bandwidth of 143.39%. Similarly, a wearable UWB MIMO antenna was proposed, covering a frequency range of 1.71–12.63 GHz, meeting the bandwidth demands for multiple applications including WiMAX, WLAN, and C-band[34]. While both designs are compact, flexible, and exhibit low SAR, their wideband designs may lead to inefficient spectrum utilization, as they cover a broad range of frequencies that may not be necessary for specific applications. The authors in[35] presents a wideband, low-profile wearable antenna operating at the 2.45 GHz WBAN band, with a CPW-fed monopole integrated with an AMC for improved bandwidth and efficiency. The design offers 71.03% impedance bandwidth (1.87–3.93 GHz), 3.62 dBi gain, and demonstrates stability and low SAR under body loading for wearable applications. However, modern wireless systems require dual- or multiband antennas, which provide better frequency flexibility and efficiency for diverse applications. Similarly, the annular-slot circular patch antenna in[36] achieves dual-band operation but compromises wearability due to rigid-textile hybrids and coaxial feeding. Recent advances in all-textile multiband designs, such as the slot-loaded circular patch in[37], prioritize comfort but suffer from low gain across operational bands.

In this paper, we propose a compact, dual-band wearable antenna inspired by the form factor of a medical syringe and optimized using machine learning techniques for efficient deployment in Wireless Body Area Network (WBAN) applications. The increasing demand for reliable, high-performance, and ergonomically adaptable antennas in healthcare monitoring systems drives the need for innovative designs that ensure both electrical efficiency and user safety. By employing machine learning—specifically supervised regression models—to predict antenna reflection characteristics, we aim to accelerate the design process and enhance performance predictability. Furthermore, the use of a flexible Rogers Duroid 3003™ substrate, along with extensive SAR and bending performance validations, highlights the antenna's practical suitability for real-world, on-body environments. This study addresses the critical need for intelligent, safe, and reliable antenna solutions in next-generation wearable biomedical systems.

Existing research on dual-band wearable antennas for WBANs faces critical limitations, including reliance on time-consuming, trial-and-error design processes that inadequately balance competing objectives like miniaturization, dual-band efficiency, and robustness to body interactions. Conventional designs often lack adaptive strategies to mitigate performance degradation caused by dynamic human body effects like tissue heterogeneity, movement, and moisture, leading to detuning and efficiency loss in real-world scenarios. While ML has shown promise in antenna design, its potential remains underexplored in optimizing ultra-compact geometries while simultaneously ensuring performance stability for WBAN applications. Compounding these challenges is the scarcity of comprehensive datasets that incorporate anatomical diversity and environmental variability, limiting the generalizability of existing models and hindering progress toward reliable, deployable wearable antenna solutions.

The integration of machine learning (ML) in antenna design has become crucial for optimizing complex, multi-objective challenges, such as miniaturization, dual-band efficiency, and performance stability in real-world scenarios[39–41]. ML techniques, particularly supervised regression models, facilitate faster design iterations, and predictive performance evaluations which are often overlooked in traditional antenna design methods[42,43]. Recent research highlights ML's potential to enhance the efficiency and reliability of wearable devices, especially for WBAN applications, where dynamic body interactions and anatomical diversity must be accounted for[44].

This paper highlights the following novel contributions:

i. A compact, wearable patch antenna (30×48.8 mm^2) is developed on a Rogers substrate, enabling operation in two frequency bands centered at 2.4 GHz and 5.8 GHz. This design resolves the inherent conflict between achieving miniaturization and maintaining robust dual-band performance.
ii. Machine learning, specifically Random Forest models, is leveraged to predict resonance frequencies and optimize geometric parameters. This method reduces computational time by 70% compared to conventional CST Microwave Studio (MWS) simulations, enabling efficient exploration of dual-band configurations.
iii. The antenna's operational stability is tested under bending conditions using a human tissue-mimicking phantom, and its SAR limits are evaluated for on-body deployment. Simulations and measurements are systematically cross-verified, providing critical insights into real-world usability, an aspect frequently neglected in earlier research.

Approach to the antenna design

The antenna design presented here draws inspiration from the structural form of a medical syringe, characterized by a slender vertical body, a finger rest, and a plunger head. This syringe-like geometry not only offers a compact and easily integrable profile but also enables efficient current distribution along the radiating elements. The vertical shaft mimics the needle pathway to facilitate directed radiation, while the horizontal arms enhance impedance matching and bandwidth performance. The unique syringe-inspired configuration combines both aesthetic simplicity and functional effectiveness, rendering it ideal for modern wireless communication applications. Moreover, designing a compact and effective antenna for WBAN applications is a major issue. Conventional antenna designs, notably rectangular patch antennas, require larger sizes to produce resonance at lower frequencies, such as 2.4 GHz. A rectangular patch antenna operating at this frequency typically requires a dimension close to one-quarter of the wavelength ($\lambda/4$). To solve this difficulty, this work employs a planar monopole design method. Initially, the antenna design arrangement was based on the fundamental microstrip-fed antenna. The patch size, including length and width, is determined via a transmission line model detailed in[45]. The CST Microwave Studio software, a finite-integration-based solver for 3D EM modeling, is employed to explore and optimize parameters related to the designed antenna. Initial designs were simulated, and the patch's length and width were repeatedly changed based on the reflection coefficient (S_{11}) results. Figure 2 illustrates the finalized antenna structure and dimensions on Rogers RO3003™ material (relative permittivity $\epsilon_r = 3$, thickness = 0.5 mm, loss tangent = 0.0013). Table 1 summarizes the optimized parameter values for the antenna.

Two separate phases of iterative development were used to develop the modelled antenna design, each of which marked a major advancement in the direction of peak performance. The progressive evolution of the suggested antenna through S_{11} analysis is depicted in Fig. 3. Strategic changes to the antenna's configuration were

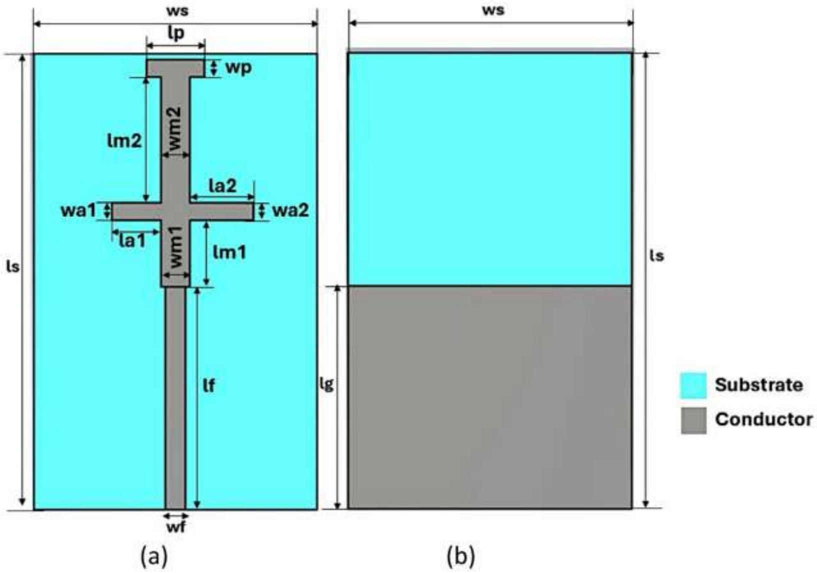

Fig. 2. Antenna design layout: (**a**) Upper side (**b**) Lower side.

Design Variables	l_s	w_s	l_p	w_p	l_f	w_f	l_g	l_{a1}	w_{a1}	l_{a2}	w_{a2}	l_{m1}	w_{m1}	l_{m2}	w_{m2}
Values (mm)	48.8	30	7	1.9	23.4	1.7	23.4	4.5	1.8	5.5	1.8	7	2.4	13.2	3

Table 1. Key parameters of the designed antenna.

made at each stage based on a thorough examination of simulation findings and performance data. A methodical investigation of design options and the identification of crucial elements impacting antenna performance were made possible by this iterative process. Each iteration's insights guided later improvements, which resulted in a slow convergence toward the intended performance goals. In the first design stage, a T-shaped monopole was employed to target a resonance at 5.8 GHz, as shown in Fig. 3a. However, due to suboptimal performance, a second design stage was initiated. This involved incorporating a rectangular monopole, as shown in Fig. 3b. The rectangular monopole was strategically positioned to introduce an additional resonance near 2.4 GHz, although it caused a shift in the upper resonant frequency. This modification effectively increased the antenna's electrical length, enabling dual-frequency resonance. While performance improved, the design still fell short of the desired outcomes. In the final stage, additional adjustments were made: a vertical monopole was introduced at the upper part of the structure, as shown in Fig. 3c, giving the antenna its characteristic medical syringe-like shape. This enhancement optimized the surface current pattern and strengthened the coupling of the two resonant frequencies. Consequently, the antenna achieved a significant bandwidth increase, enabling efficient operation across a wider spectrum without compromising its dual-band operation. Accordingly, it resonates efficiently at two specific operational frequencies, demonstrating improved reflection coefficients and enhanced performance. Through this process of iterative refinement, the antenna design evolved not only structurally but also conceptually, highlighting the transformative power of iterative design in antenna engineering.

Parametric investigation

An extensive parametric analysis was performed to examine how varying the length of the partial ground plane influences the antenna's functional response. The effects of these parameter adjustments on antenna behavior are illustrated in Fig. 4. As illustrated in the figure, increasing the length of the partial grounding surface (lg) raises the resonant frequency. By maintaining lg within the 15.5 to 23.4 mm range, the desired upper band of 5.8 GHz with an optimal S_{11} is achieved at lg = 23.4 mm. This implies that the antenna utilizes a truncated ground rather than an entire ground plane, indicating that the grounding surface significantly influences the antenna's operational characteristics.

Figure 5 illustrates the parametric analysis conducted to evaluate the influence of la1 and la2 on the lengths of the T-shaped radiating arms on the antenna's performance. A systematic optimization study was performed by varying la1 and la2 across a range of 2.8 mm to 5.5 mm to identify their impact on impedance matching and resonant frequency behavior. The findings indicate that the antenna attains an optimal S_{11} at la1 = 4.5 mm and la2 = 5.5 mm, enabling the desired higher frequency band centered at 5.8 GHz. This configuration ensures minimal signal loss and robust bandwidth performance.

A systematic parametric investigation was performed to determine the optimal length (lp) on the upper T-shaped patch of the proposed antenna and its influence on critical performance metrics, including resonant

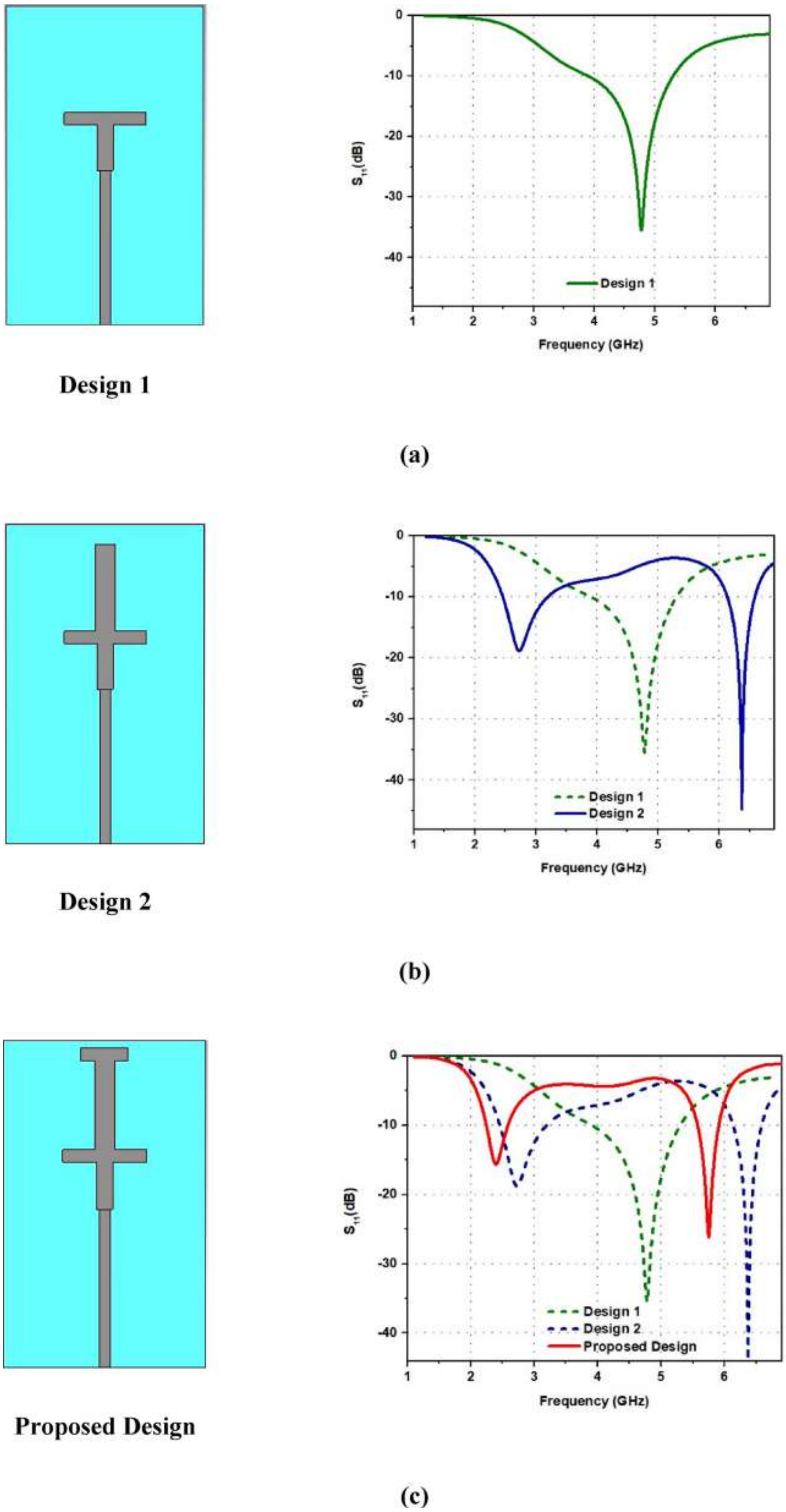

Fig. 3. Progressive design refinement of the antenna through S_{11} analysis.

frequency, impedance matching, and operational bandwidth. This analysis aimed to identify the ideal lp configuration that maximizes the antenna's efficiency and frequency response. Simulations were conducted across a sweep of lp values (1 mm to 7 mm), with results illustrated in Fig. 6. The study reveals a direct correlation between lp and resonant frequency shifts: as lp increases, the antenna's electrical length elongates, lowering the resonant frequency. However, the optimal S_{11} < -10 dB, indicating minimal signal reflection and

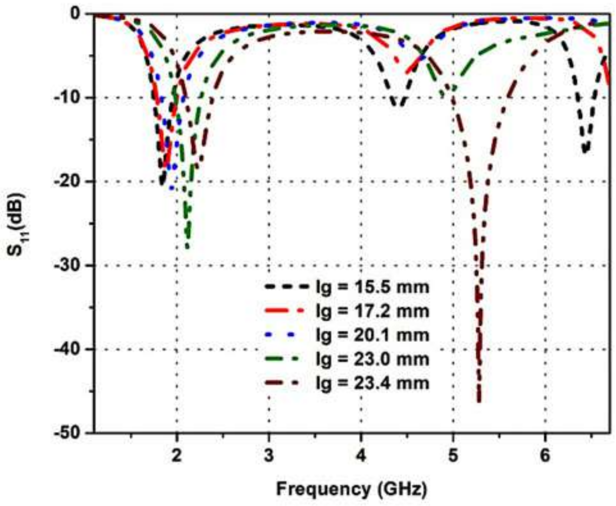

Fig. 4. Effect of S_{11} with changes in lg.

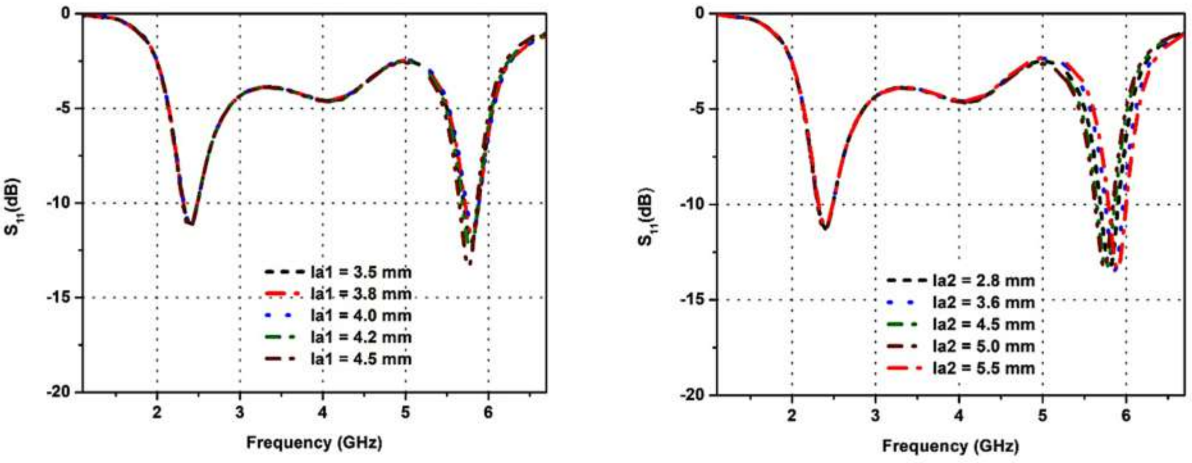

(a)

(b)

Fig. 5. Effect of S_{11} with changes in (**a**) la1 (**b**) la2.

effective impedance matching, is achieved at lp = 7 mm, which stabilizes the antenna's upper frequency band while maintaining a broad operational bandwidth.

Figure 7 presents a parameter study of the designed antenna, focusing on the influence of wf (feedline width) and wa1 (width of the T-shaped radiating arm) on its performance. A systematic parametric optimization study was conducted by sweeping wf and wa1 across a range of 0.3 to 2.0 mm to evaluate their effects on impedance matching, bandwidth, and resonant frequency behavior. The results demonstrate that adjustments to these parameters significantly alter the antenna's electromagnetic response. Specifically, the optimal configuration achieving $S_{11} < -10\,dB$, indicating efficient impedance matching and low transmission loss, is observed at wf = 2.0 mm and wa1 = 1.8 mm. This configuration stabilizes the antenna's upper frequency band at 5.8 GHz. Notably, reducing wf below 3.0 mm increases feedline resistance, degrading the S_{11} performance, while widening wa_1 beyond 2.2 mm introduces parasitic resonances, fragmenting the operational bandwidth. Conversely, values smaller than wa1 = 1.8 mm shift the resonant frequency upward but compromise radiation efficiency. The study highlights the sensitivity of the T-shaped geometry to dimensional precision, where even minor deviations from the optimized wf and wa1 values disrupt the antenna's frequency response. These results emphasize the prominence of balancing feedline and arm dimensions to achieve targeted bandwidth and resonance characteristics in compact antenna designs.

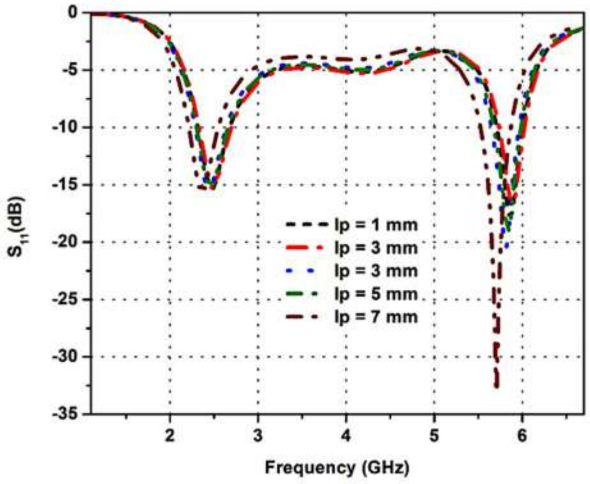

Fig. 6. Effect of S_{11} with changes in lp.

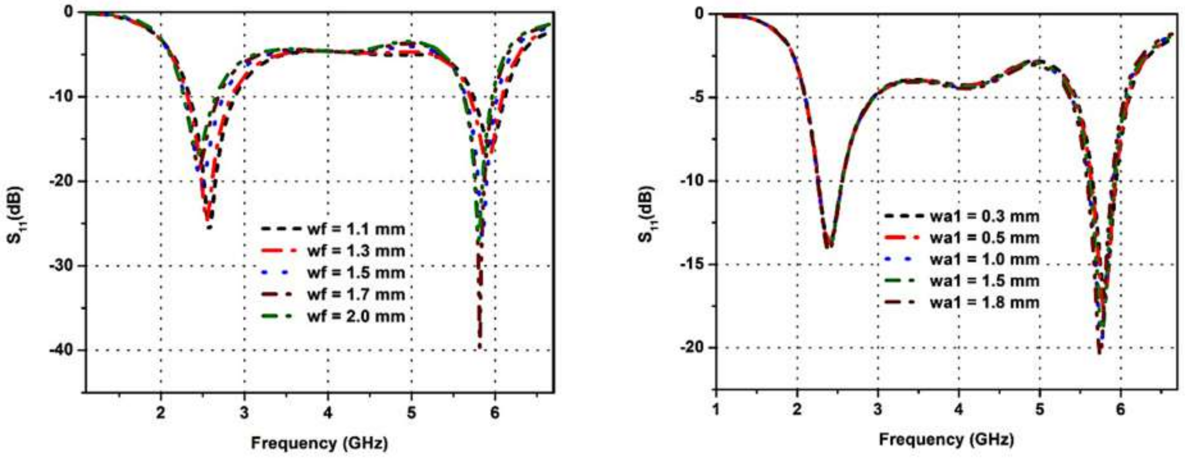

(a) (b)

Fig. 7. Effect of S_{11} with changes in (**a**) wf (**b**) wa1.

Equivalent circuit model

Before conducting detailed simulations or experimental testing, an equivalent circuit model provides a beneficial validation methodology in the antenna design process. It facilitates preliminary assessment of essential antenna characteristics, including bandwidth, impedance matching, and resonant frequency. In this study, the S_{11} data is extracted using Advanced Design System (ADS) software for model optimization and is subsequently compared with simulation results obtained from CST MWS to validate accuracy and consistency. The microstrip patch antenna under investigation behaves similarly to an open-ended transmission line, a characteristic that facilitates its modeling through lumped circuit elements. The equivalent circuit model of the modelled dual-band antenna, illustrated in Fig. 8, provides a simplified yet insightful representation of the antenna's electrical behavior. This model consists of three primary sections: the feed network and two resonant branches corresponding to the antenna's dual operating bands. The feed network includes a coaxial SMA port and associated circuit elements impedance (Z_p), capacitance (C_f), inductance (L_f), and resistance (R_f). This section is critical for efficient signal excitation, impedance transformation, and minimization of reflection and insertion loss at the input. To replicate the dual-band functionality, two parallel RLC resonant circuits are incorporated into the model[46]. The equivalent circuit parameters were first estimated from closed-form resonance equations and quality factor relations and subsequently refined by curve fitting to match the CST-simulated S_{11} response. This ensured that the equivalent circuit accurately reproduced both the lower and upper resonances of the antenna. The first RLC branch comprising L_1, C_1, and R_1 represents the resonance at the lower band around 2.4 GHz. The second RLC branch comprising L_2, C_2, and R_2 models the resonance at the higher band near 5.8 GHz. Each RLC circuit captures the corresponding resonance behavior, including bandwidth characteristics and quality factor, thereby

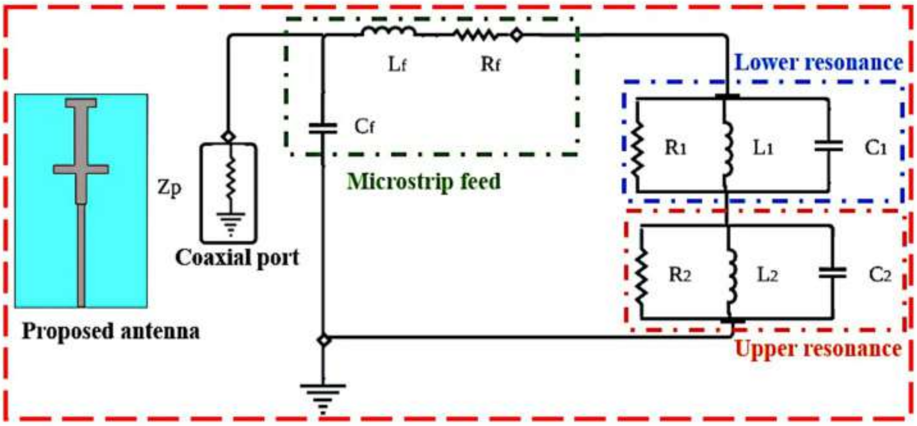

Fig. 8. Equivalent circuit parameters: Zp = 50.9 Ω, Cf = 2.7 pF, Lf = 5.6 nH, Rf = 7.6 Ω, L1 = 4.8 nH, C1 = 32 pF, R1 = 56 Ω, L2 = 9.3 nH, C2 = 0.7 pF, R2 = 54 Ω.

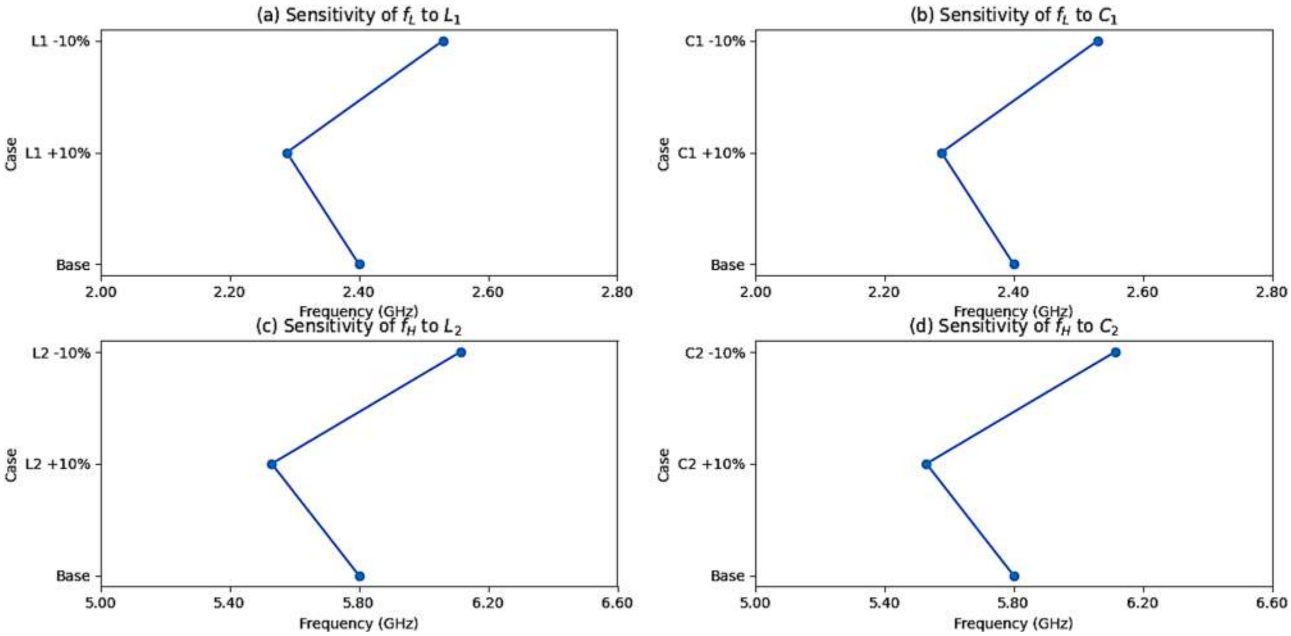

Fig. 9. Sensitivity plots of the equivalent circuit model showing the effect of ± 10% variations in circuit parameters on the resonant frequencies: (**a**) L_1 on f_L, (**b**) C_1 on f_L, (**c**) L_2 on f_H, and (**d**) C_2 on f_H.

accurately emulating the antenna's performance in both frequency bands. Overall, the use of the equivalent circuit modeling method provides a foundational understanding of the antenna's behavior, facilitating faster optimization and deeper insight into its two-band functionality at 2.4 GHz and 5.8 GHz.

To examine the robustness of the extracted equivalent circuit, a sensitivity analysis was carried out by varying $\frac{L_1}{C_1}$ for the lower resonance (f_L) and $\frac{L_2}{C_2}$ for the upper resonance (f_H) by ± 10%. The results, shown in Fig. 9, indicate that increasing either L_1 or C_1 by 10% shifts the lower resonance downward from 2.40 GHz to approximately 2.28 GHz, while decreasing them by 10% shifts it upward to about 2.53 GHz. A similar trend is observed for the upper resonance, where increasing L_2 or C_2 by 10% reduces f_H from 5.80 GHz to roughly 5.54 GHz, and decreasing them by 10% raises it to nearly 6.17 GHz. These shifts are consistent with the expected inverse square-root dependence of resonance frequency on the LC product, thereby confirming both the physical plausibility and the reliability of the equivalent circuit parameter extraction.

Antenna optimization using machine learning

Traditional optimization methods in antenna design such as parameter sweeps, genetic algorithms, and particle swarm optimization have been employed for decades. While effective for simpler designs, these techniques falter when applied to the growing complexity of modern antenna systems[47,48]. Advances in wireless technologies, including 5G/6G networks, IoT, medical imaging, and vehicular radar, demand antennas with higher performance, multifunctionality, and compact form factors. These requirements have spurred the development of intricate designs capable of supporting multiband operation, integrating advanced features like MIMO (Multiple-Input Multiple-Output) and beam steering, and embedding components such as slots, impedance transformers, and defected ground structures. However, optimizing these sophisticated geometries is challenging with conventional methods. Optimizations often necessitate full-wave electromagnetic (EM) simulations, which are computationally intensive and time-consuming. As antenna topologies grow more complex, traditional optimization algorithms struggle to balance precision with efficiency, leading to prohibitive computational costs and suboptimal performance. ML has emerged as a transformative alternative. By modeling the relationship between antenna geometry and performance, ML-driven approaches enable rapid optimization while reducing reliance on costly EM simulations. This paradigm shift streamlines the design process, facilitating faster, more accurate tuning of complex antenna systems[49].

Machine learning (ML) approaches in antenna optimization typically involve techniques like reinforcement learning (RL), semi-supervised learning (SSL), unsupervised learning (UL), and supervised learning (SL). Among these, SL is the most prevalent in antenna design due to its capacity to map input parameters to desired outputs using labelled datasets. However, its reliance on extensive labelled data remains a limitation. Nevertheless, challenges such as overfitting on limited datasets, lack of physical interpretability of ML models, and difficulties in validating predictions against full-wave solvers and measurements remain open issues in this domain. To mitigate this challenge, surrogate models developed using ML methods like artificial neural networks (ANNs), support vector machines (SVMs), and regression analysis have gained much attention by researchers. These models bypass time-consuming electromagnetic (EM) simulations by predicting antenna performance directly from geometric or material parameters, significantly accelerating the design process while maintaining accuracy. This study employs ML algorithms to predict the resonant frequency of antennas directly from their geometric parameters. By training ML models to estimate the resonant frequency of the antenna, the proposed approach bypasses computationally expensive full-wave electromagnetic (EM) simulations. This enables rapid, accurate performance predictions and simplifies the antenna optimization process.

The training datasets were generated from the antenna modeled and optimized in CST Studio Suite using Genetic Algorith (GA), as detailed in Sect. 3. The GA was chosen for its effectiveness in resolving nonlinear, multi-variable optimization challenges inherent to antenna geometry tuning. Key geometric inputs included lower T-shaped Monopole dimensions (la1, wa1), ground plane length (lg), substrate dimensions (ls, ws), and dimensions of the upper T-shaped monopole (lp, wp). Corresponding outputs (resonant frequencies) were recorded for 8,009 unique configurations generated through parametric sweeps. This dataset size balances design-space coverage with computational feasibility. The dataset was shuffled and split into 80% for training, 10% for validation, and 10% for testing. To identify the optimal predictor, several regression algorithms were evaluated: random forests, decision trees, Gaussian process, nearest neighbour, and support vector machine (SVM). These were selected for their ability to model nonlinear relationships, handle high-dimensional inputs, and mitigate overfitting critical traits for robust S_{11} prediction.

Figure 10 illustrates a systematic workflow for predicting resonant frequency using ML algorithms. The process begins by training ML models on a labelled dataset to map geometric input variables to the target resonant frequency. Following training, models are evaluated on a holdout test dataset, where predictions are compared against ground-truth values using error metrics (e.g., root mean squared error, mean absolute error) and goodness-of-fit measures (e.g., R^2 score). Models failing to meet predefined accuracy thresholds are iteratively replaced with alternative regression algorithms, while top-performing candidates advance to deployment. The finalized model is then applied to new, unseen data, harnessing learned patterns to deliver reliable resonant frequency predictions. The effectiveness of the model was rigorously assessed through statistical metrics such as MAE, RMSE, and R^2, which are summarized in Table 2, along with their corresponding mathematical formulation.

Figure 11 evaluates the prediction accuracy of the tested algorithms using error metrics (MAE, MSE, MSLE, RMSLE, RMSE) for resonant frequency estimation. Figure 12 complements this analysis with R^2 scores, quantifying each model's goodness-of-fit, while Fig. 13 offers a comparison of predicted frequency plots for the proposed antenna using CST MWS simulation against the actual simulated results obtained from different regression models. The random forest model outperformed others, achieving the lowest error rates (MAE: 0.35, MSE: 0.89, MSLE: 0.21, RMSLE: 0.35, RMSE: 0.94) and the highest R^2 value (87.70%). These results demonstrate Random Forest's superior ability to minimize prediction discrepancies and capture complex relationships between geometric parameters and resonant frequency, solidifying its efficacy for antenna performance optimization.

The Random Forest model was optimized using Bayesian Hyperparameter Optimization, aiming to strike a balance between model complexity and computational efficiency. This optimization led to the identification of the following best hyperparameters as presented in Table 3

These hyperparameters enhanced the model's performance and ensured it effectively managed nonlinear relationships in the data without overfitting. By using the Random Forest algorithm, the model was able to capture complex patterns in the dataset and maintain generalization across various scenarios. To ensure reproducibility, the random seed was set to 42. Training data was used to train the model, while the validation set helped in tuning hyperparameters through Bayesian optimization. The test set provided the means to evaluate the model's final performance, with metrics such as R^2 and other error indicators being calculated for assessment. For the training and validation process, Bayesian Search Cross-validation (BayesSearchCV) was employed. This technique was utilized to efficiently search for the best hyperparameters by focusing on minimizing the Mean Absolute Error (MAE) and maximizing R^2. Compared to the traditional grid search method, this approach reduced computational time by 70%, significantly accelerating the hyperparameter tuning process when

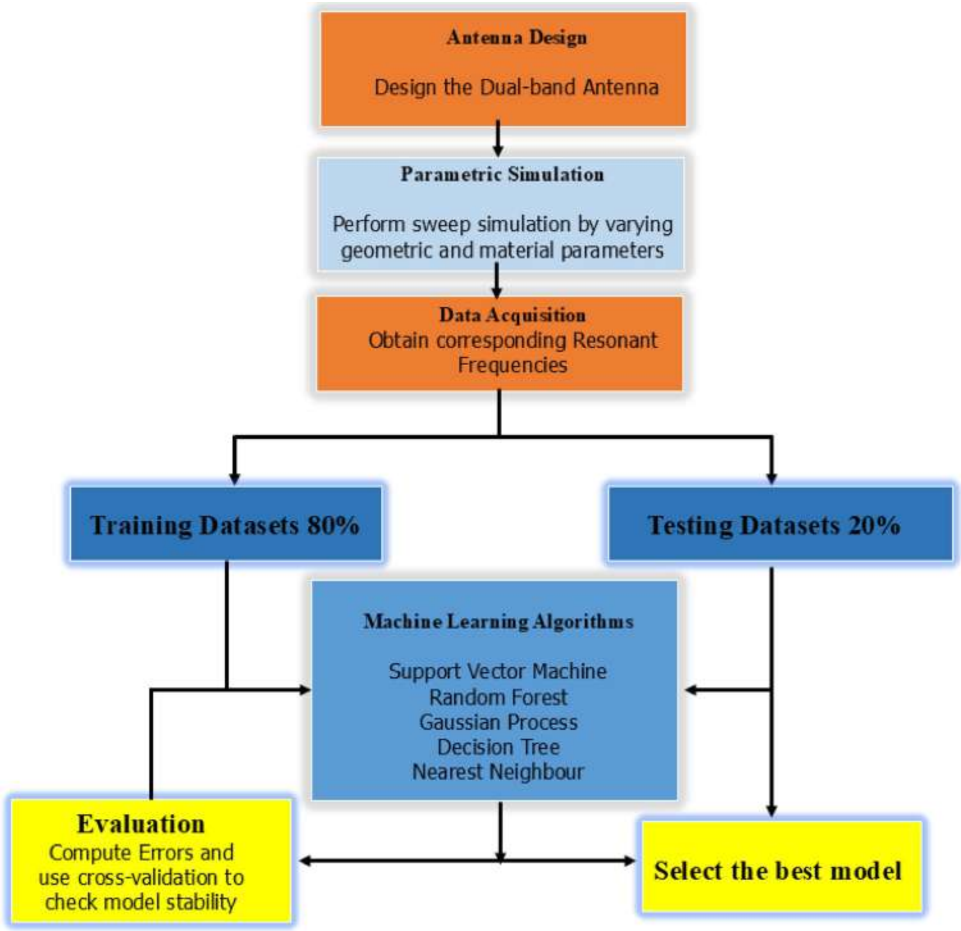

Fig. 10. Flowchart showcasing the ML optimization process for resonant frequency prediction.

Error	Mathematical formulation
Mean squared logarithmic error (MSLE)	$\frac{1}{n}\sum_{i=1}^{n}\left(\log(1+y_i)-\log\left(1+\widehat{y_i}\right)\right)^2$
Root mean squared logarithmic error (RMSLE)	$\sqrt{\frac{1}{n}\sum_{i=1}^{n}\left(\log(1+y_i)-\log\left(1+\widehat{y_i}\right)\right)^2}$
Variance score (R-squared)	$1-\frac{\sum_{i=1}^{N}\left(y_i-\widehat{y_i}\right)^2}{\sum_{i=1}^{N}\left(y_i-\bar{y}\right)^2}$
Mean absolute error (MAE)	$\frac{1}{n}\sum_{i=1}^{n}\left\lvert y_i-\widehat{y_i}\right\rvert$
Mean absolute percentage error (MAPE)	$\frac{1}{n}\sum_{i=1}^{n}\left\lvert\frac{y_i-\widehat{y_i}}{y_i}\right\rvert\times 100\%$
Root mean squared error (RMSE)	$\sqrt{\frac{1}{n}\sum_{i=1}^{n}(P_i-O_i)^2}$
Mean squared error (MSE)	$\frac{1}{n}\sum_{i=1}^{n}\left(y_i-\widehat{y_i}\right)^2$

Table 2. Performance metrics for regression analysis.

compared to conventional CST Microwave Studio (MWS) simulations. The performance of the Random Forest model was evaluated based on some key metrics as depicted in Table 4.

These performance metrics reflect the strong predictive capability of the model, with an R^2 value of 0.877 indicating a high level of accuracy in predicting unseen data. In terms of model runtime, the optimized Random Forest model demonstrated a significant reduction in training time compared to the traditional CST MWS

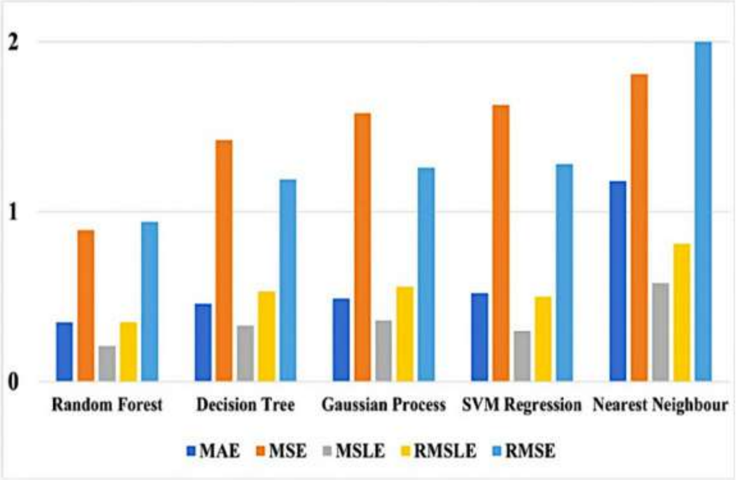

Fig. 11. Comparison of various ML algorithms and their corresponding errors in predicting S_{11}.

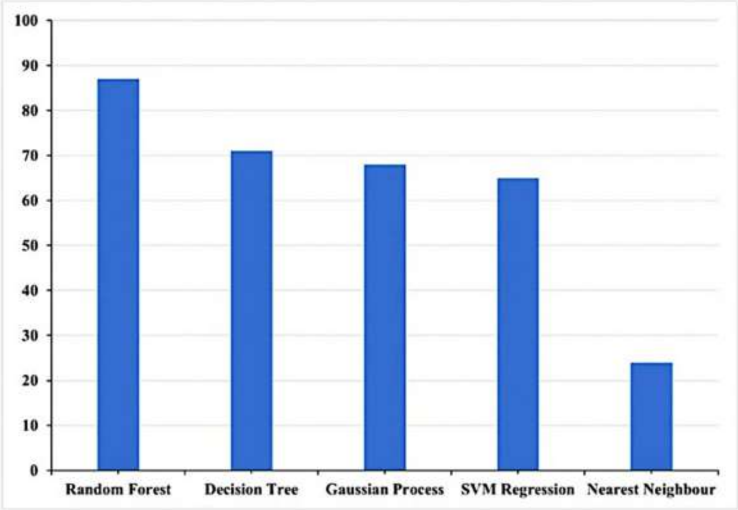

Fig. 12. Accuracy plots showing the R^2 values of various ML algorithms in predicting S_{11} performance.

simulations. Table 5 compares the per-epoch training time and total wall-time between the two approaches, showing that the optimization techniques resulted in a 70% faster process.

Figure 14 presents the plot of the Learning Curve and Parity plot for the Random Forest model. The Learning Curve in Fig. 14a illustrates the steady improvement in the Mean Absolute Error (MAE) over 100 epochs of training, with the MAE consistently decreasing, indicating that the model was effectively learning and converging. The R^2 value of 0.877 further reflects the model's strong performance during training. In Fig. 14b, the Parity Plot compares the predicted resonant frequencies to the actual frequencies from the test set, demonstrating excellent predictive accuracy. The R^2 value of 0.989 confirms that the Random Forest model can reliably predict resonant frequencies based on the antenna's geometrical parameters, showcasing both robust training and high predictive capability.

The RF model was evaluated using 5-fold cross-validation to obtain cross-validated performance metrics. The Mean Absolute Error (MAE) and Root Mean Squared Error (RMSE) were calculated, and their respective 95% Confidence Intervals (CI) were computed. The results from cross-validation revealed an average MAE of 4.0352, with a 95% CI of (3.2521, 4.8183), and an average RMSE of 2.3711, with a 95% CI of (2.1084, 2.6337). These results indicate that the Random Forest model performed consistently across different folds, with narrow confidence intervals suggesting stable performance in generalizing to unseen data. The plots in Fig. 15 illustrate the distribution of the Mean Absolute Error (MAE) and Root Mean Squared Error (RMSE) across the cross-validation folds and highlight the consistency and robustness of the model's performance. The MAE values were predominantly observed in the range between 4 and 10, and RMSE values mostly fell between 2.4 and 3.4, with no significant outliers detected. This further supports the robustness of the model. When the model

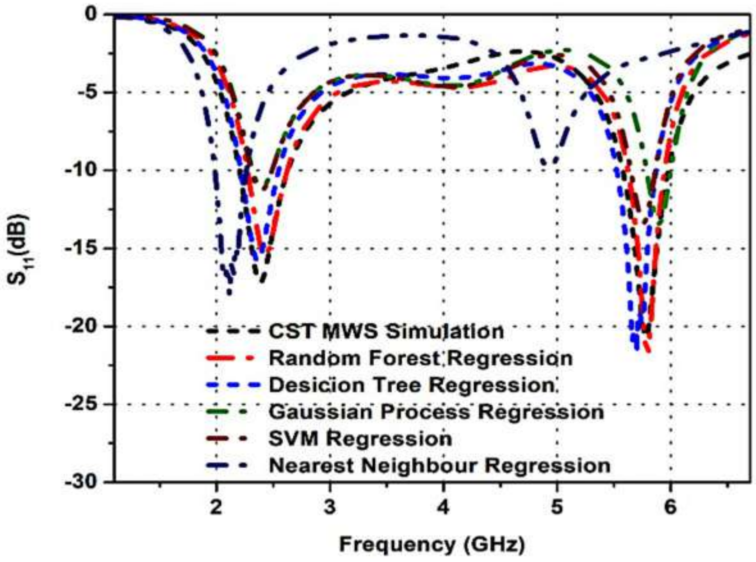

Fig. 13. Performance comparison of CST MWS simulations for various models with ML-based predictions.

Hyperparameter	Value
max_depth	15
min_samples_leaf	1
min_samples_split	2
n_estimators	423

Table 3. Hyperparameters of the best model.

Metric	Result
R^2 (Test Set)	0.877
Root mean squared error (RMSE)	3.79
Mean absolute error (MAE)	2.91

Table 4. Performance of the random forest model.

Metric	Random Forest (Optimized)	CST MWS Simulation (Baseline)
Per-epoch training time	0.015 s/epoch	N/A
Total wall-time	18 min	1.5 h
Time reduction	-	70% faster

Table 5. Comparison of the per-epoch training time with total wall-time.

was evaluated on the test set, an R^2 score of 0.7786 was obtained, confirming that the model was effective in explaining the variance in the data and in generalizing well to unseen data.

Results and discussions

The proposed antenna prototype, illustrated in Fig. 15, was fabricated to validate the design and simulation results. A standard 50 Ω SMA connector was employed to excite the structure. Its characteristics were assessed using a Keysight Analyzer and measurements conducted in a calibrated anechoic chamber. The following subsections detail the experimental findings, including S_{11}, current distribution on the surface of the antenna, radiation characteristics, gain, and overall efficiency. For each parameter, a thorough comparison of simulated versus measured data is provided to confirm the antenna's performance.

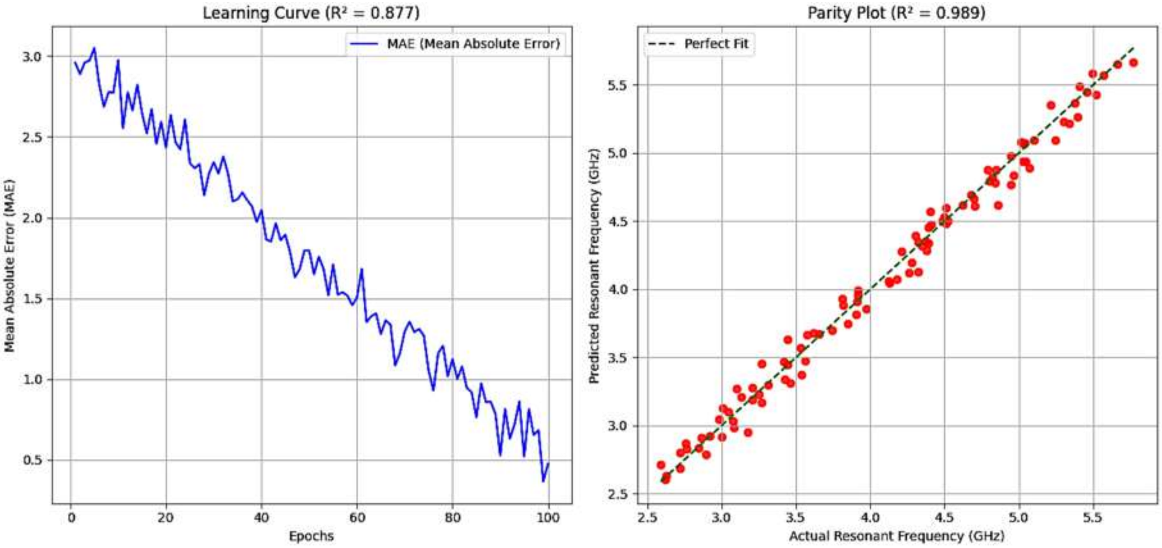

(a) (b)

Fig. 14. (**a**) Learning Curve and (**b**) Parity Plot of the Random Forest Model, illustrating the model's training performance and predictive accuracy.

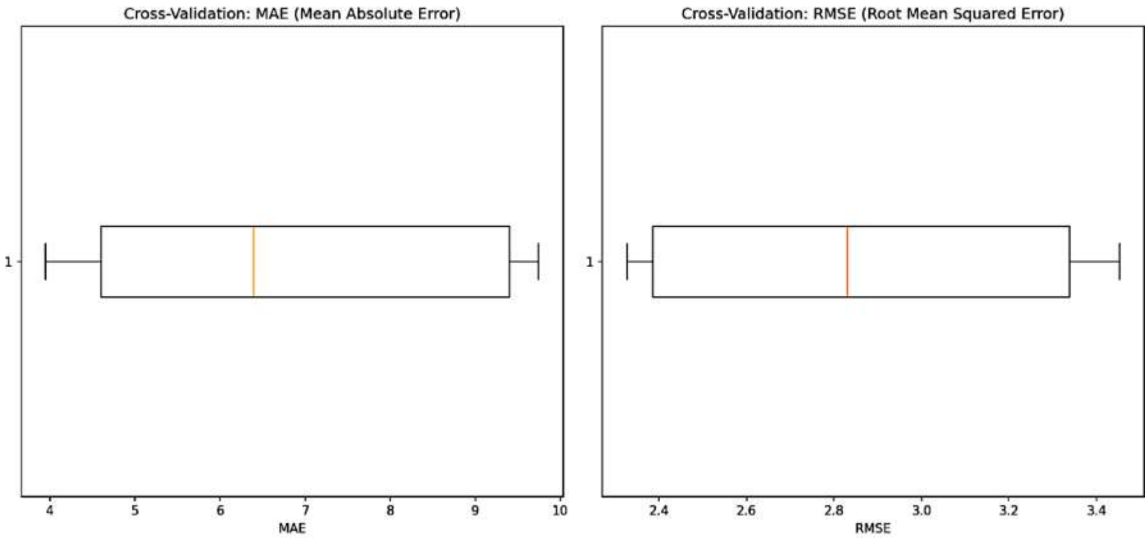

(a) (b)

Fig. 15. Distribution of (**a**) MAE and (**b**) RMSE across cross-validation folds.

Reflection coefficient

The S_{11} characteristics of the designed antenna, shown in Fig. 17, presents a comprehensive comparison among simulation results (CST MWS), equivalent circuit analysis (ADS), and measured data from the fabricated prototype. At 2.4 GHz, CST simulations indicate an S_{11} below – 10 dB across the band from 2.333 to 2.565 GHz. The corresponding higher-band resonance near 5.8 GHz, based on the ADS model, spans from 5.553 GHz to 6.013 GHz. In contrast, the simulated data show the – 10 dB return loss threshold is met from 2.358 GHz to 2.521 GHz, while the higher frequency resonance extends from 5.551 GHz to 5.932 GHz. The measured response at 2.4 GHz satisfies the – 10 dB criterion over 2.382 GHz to 2.511 GHz, and at 5.8 GHz, it ranges from 5.634 GHz to 5.911 GHz. Overall, there is a strong correlation among the simulation outputs, circuit-based predictions, and experimental findings—reinforcing the accuracy and reliability of the antenna design across different evaluation methods. This consistency validates the antenna's effectiveness for WBAN applications, fulfilling essential operational criteria for dependable performance.

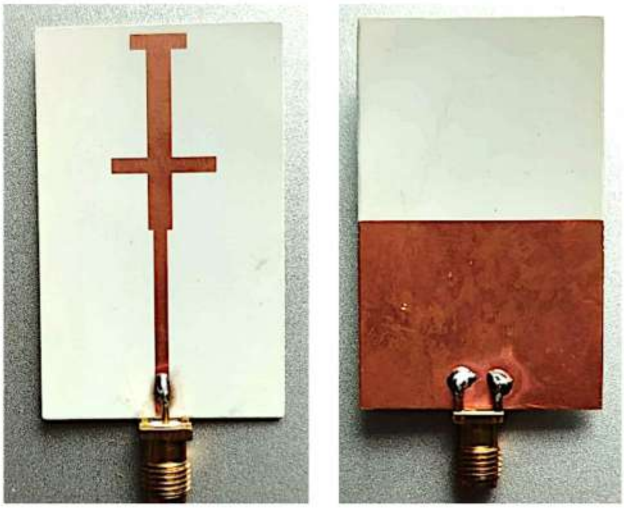

(a) (b)

Fig. 16. Manufactured antenna prototype: (**a**) Top side (**b**) Bottom side.

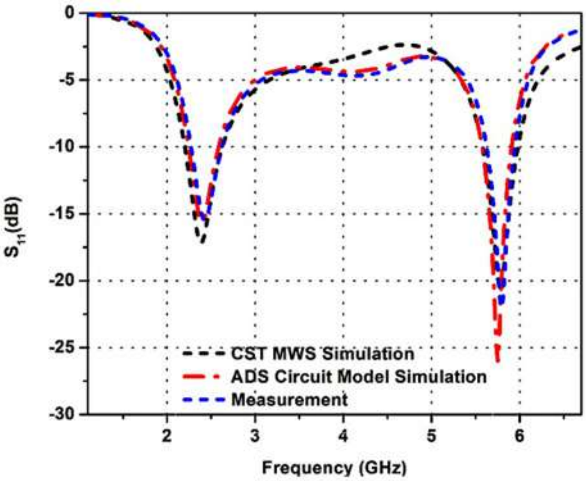

Fig. 17. Proposed antenna S_{11} based on the simulation model, measurement results and the equivalent circuit model.

Surface current distribution

The current distribution on the antenna surface reveals the areas of the antenna that are most critical in enabling operation at the resonant frequency[50]. Figure 18 illustrates the surface current distribution of the proposed antenna. At the 2.4 GHz frequency, the surface current predominantly accumulates near the feed line and along all the monopole arms, enhancing effective radiation, as illustrated in Fig. 18a. In contrast, at the upper resonance near 5.8 GHz, the peak current occurs at the lower T-shaped monopole, as illustrated in Fig. 18b. Therefore, it is evident that the feed line and all arms of the monopoles generate the first resonant frequency around 2.4 GHz, whereas the lower T-shaped monopole is responsible for the second resonance near 5.8 GHz. This observation aligns with theoretical findings in the literature[51], which suggest that the resonant frequency is influenced by the current path size across the radiating structure. Specifically, a longer current path leads to a lower resonant frequency and a shorter path results in a higher frequency.

Radiation characteristics and gain

The radiation characteristics of an electromagnetic source such as an antenna can be depicted graphically in two dimensions via a 2D radiation pattern. These patterns are critical in fields such as antenna design, telecommunications, radar systems, and others, where understanding electromagnetic wave propagation is essential[52–54]. Radiation patterns may depict radio waves, light, or microwaves. The 2D radiation characteristics

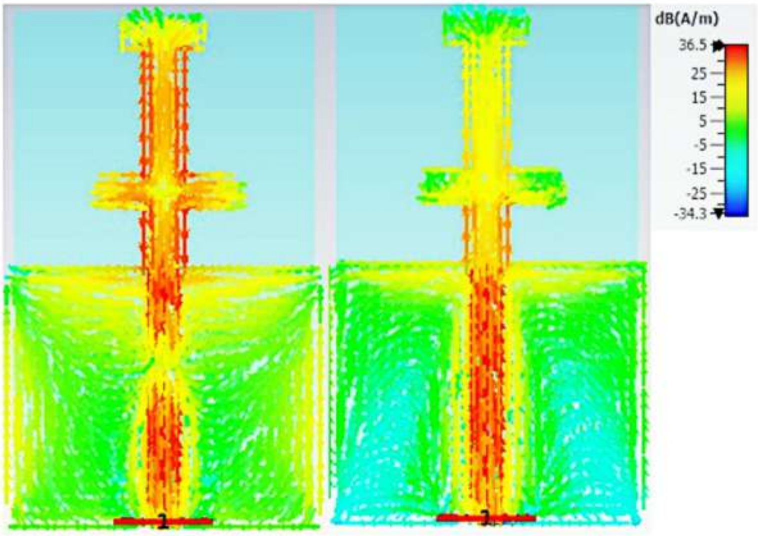

(a) (b)

Fig. 18. Surface current analysis for the proposed antenna (**a**) 2.4 GHz (**b**) 5.8 GHz.

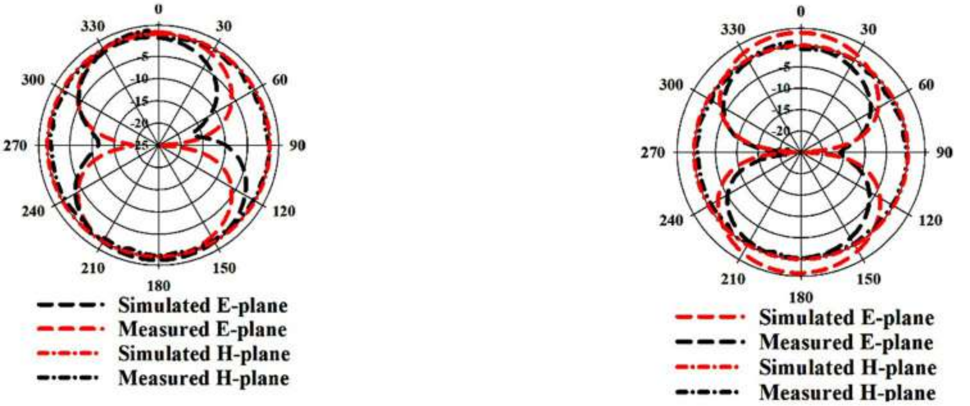

(a) (b)

Fig. 19. Radiation pattern *E*-plane (φ = 0°), and *H*-Plane (φ = 90°) as a function of θ (**a**) 2.4 GHz (**b**) 5.8 GHz.

of the electric (E-field) and magnetic (H-field) components, both simulated and experimentally measured, are presented in Fig. 19. At 2.4 GHz, the H-plane exhibits an omnidirectional pattern, ensuring reliable connectivity across all azimuthal directions, a feature that accommodates unpredictable body movements and orientations. Meanwhile, the E-plane pattern is bidirectional, concentrating energy toward specific elevation angles to minimize interference and enhance signal strength for communication with fixed base stations or wearable hubs. The measured results closely align with the simulations shown in Fig. 19a. Similarly, at 5.8 GHz (Fig. 19b), the H-plane remains omnidirectional, while the E-plane retains its bidirectional shape.

The measured antenna gains are 4.0 dBi at 2.4 GHz and 6.2 dBi at 5.8 GHz, corresponding to radiation efficiencies of 91% and 93%, respectively, as detailed in Fig. 20a, b. This indicates stable gain performance over the frequency bands of the antenna, supporting reliable signal propagation and reception.

Bending investigation

Bending is a critical factor to consider when developing wearable antennas, as real-world usage often subjects them to deformation. To assess this, the behavior of the antenna was thoroughly examined under different bending scenarios. Simulations and measurements were conducted considering deformation of the antenna along the x- and y orientations, using curvature diameters of 30, 60, and 90 mm dimensions corresponding to typical human arm and leg sizes[55]. In simulations, CST Microwave Studio (CST MWS) modeled the antenna's

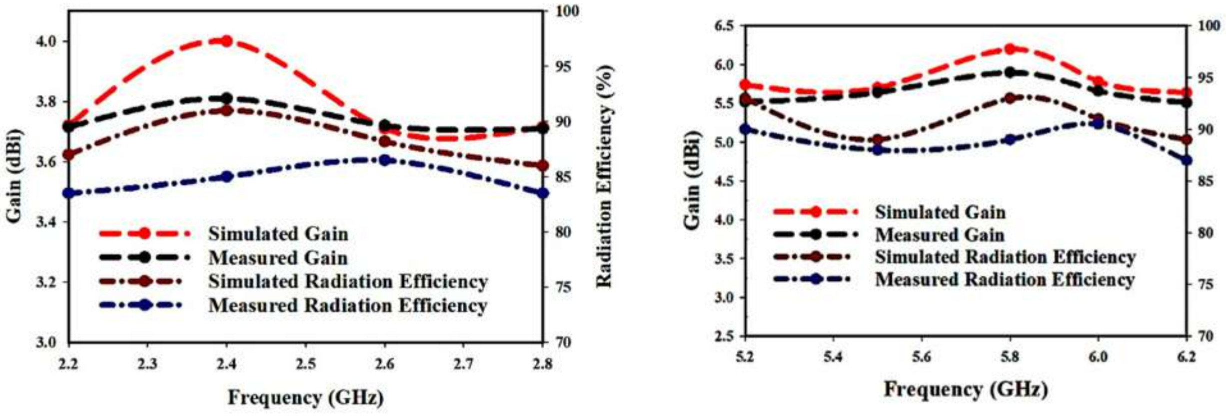

(a) (b)

Fig. 20. Gain and efficiency (**a**) 2.4 GHz (**b**) 5.8 GHz.

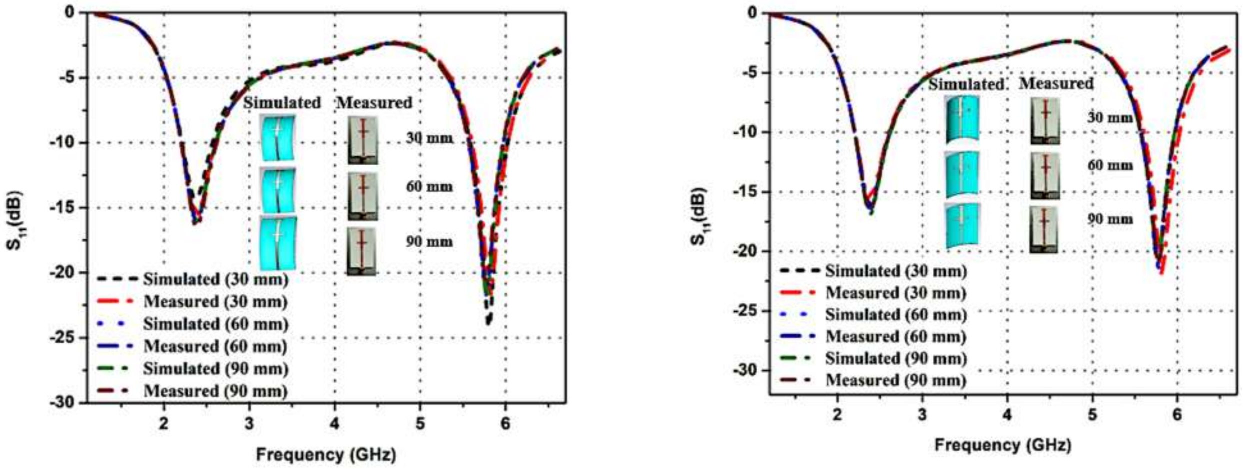

(a) (b)

Fig. 21. S_{11} under bending investigation for various diameters (**a**) x-axis (**b**) y-axis.

bending behavior by wrapping it around a vacuum cylinder, which approximates an ideal rigid cylindrical surface. Experimentally, Styrofoam was employed to physically validate the bending effects. Figure 20 compares the simulated and measured S_{11} parameters under vertical and horizontal bending. The results demonstrate stable performance across both orientations: the simulated S_{11} remains consistent, with values for the 2.4 GHz and 5.8 GHz bands consistently staying below − 10 dB, indicating minimal impact on antenna functionality.

Due to experimental constraints including limited resources, time, and equipment availability, radiation pattern measurements under bending conditions were restricted to a diameter of 90 mm. As illustrated in Fig. 22a-d, the radiation patterns maintain consistent bidirectional behavior across all tested diameters. However, a slight rise in back radiation is observed compared to the unbent state, likely caused by substrate deformation during bending. Figure 23 details the gain measurements conducted in an anechoic chamber under bending conditions. At 2.4 GHz as seen in Fig. 23a, both simulated and measured gains range between 4.2 dBi and 4.8 dBi across x-axis and y-axis. Similarly, at 5.8 GHz as seen in Fig. 23b), gains vary from 4.0 dBi to 5.2 dBi in both orientations. Despite bending, the antenna's simulated and measured gains showed no significant degradation, confirming that bending has minimal impact on efficiency and real-world operational reliability.

On-body measurement

The antenna's performance was tested in on-body configurations (chest, lap and arm) to evaluate its reliability in real-world biomedical applications. As presented in Fig. 24, the predicted S_{11} parameters are compared for placements on the chest, arm, and lap, as well as in free space. The dual-band working at 2.4 GHz and 5.8 GHz showed only slight frequency shifts, with minimal impact on functionality, as both bands consistently maintained S_{11} values below the − 10 dB threshold a critical indicator of stable impedance matching.

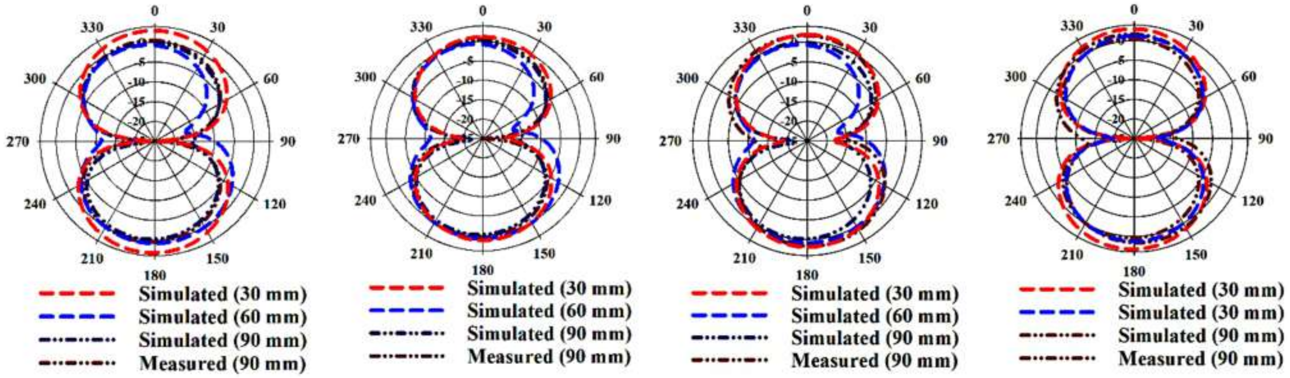

(a) (b) (c) (d)

Fig. 22. Radiation patterns (E-plane ($\varphi = 0°$) as a function of θ under bending investigation (**a**) 2.4 GHz (x-axis), (**b**) 2.4 GHz (y-axis), (**c**) 5.8 GHz (x-axis), (**d**) 5.8 GHz (y-axis).

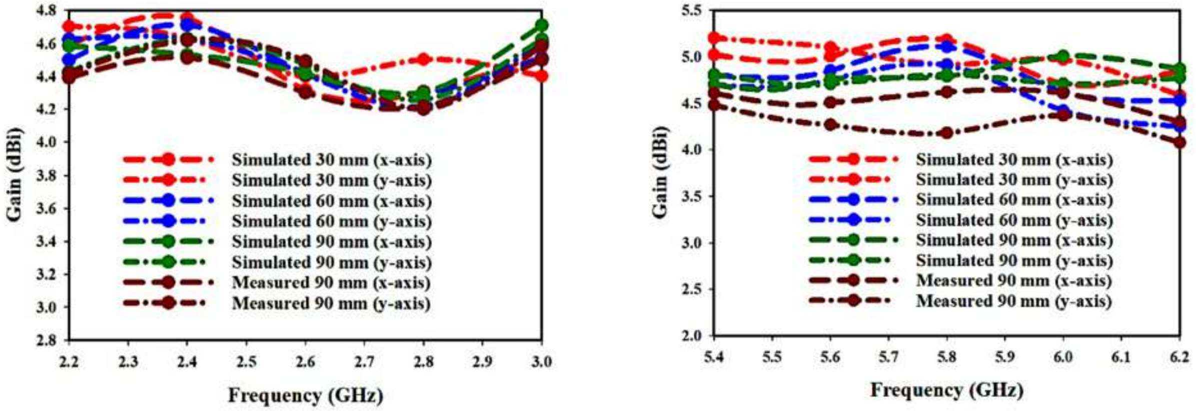

(a) (b)

Fig. 23. Gain under bending investigation (**a**) 2.4 GHz (**b**) 5.8 GHz.

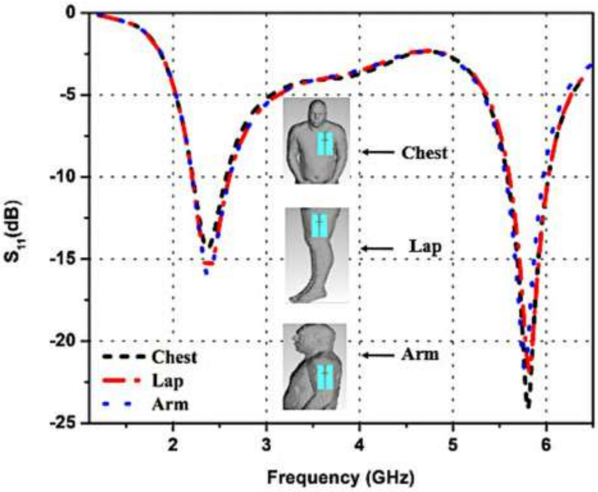

Fig. 24. Simulated S_{11} for the antenna in various body settings: Chest, lap and arm.

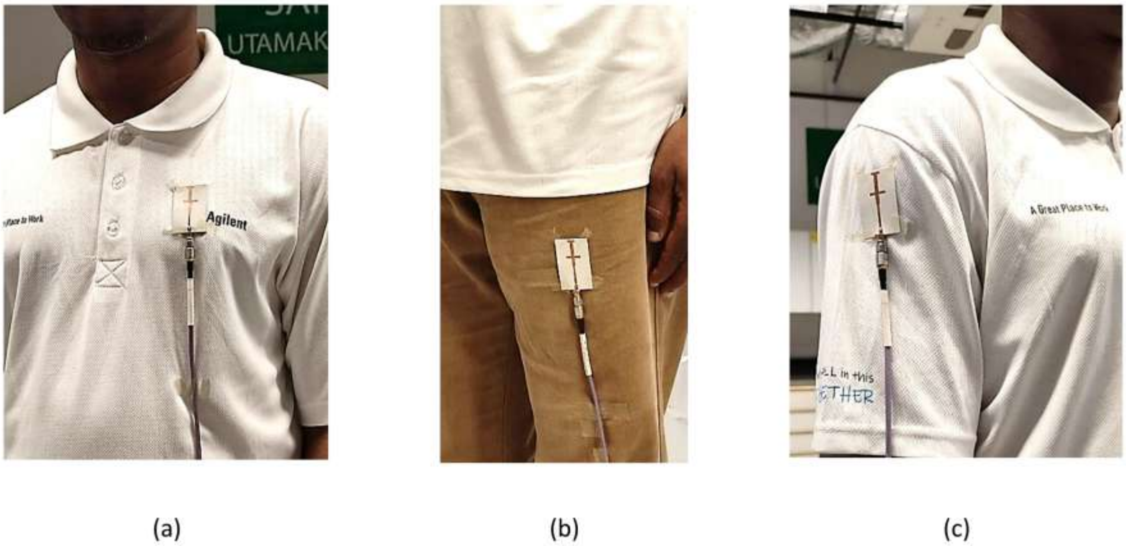

Fig. 25. Wearable antenna on various parts of human body: (**a**) chest (**b**) lap (**c**) arm.

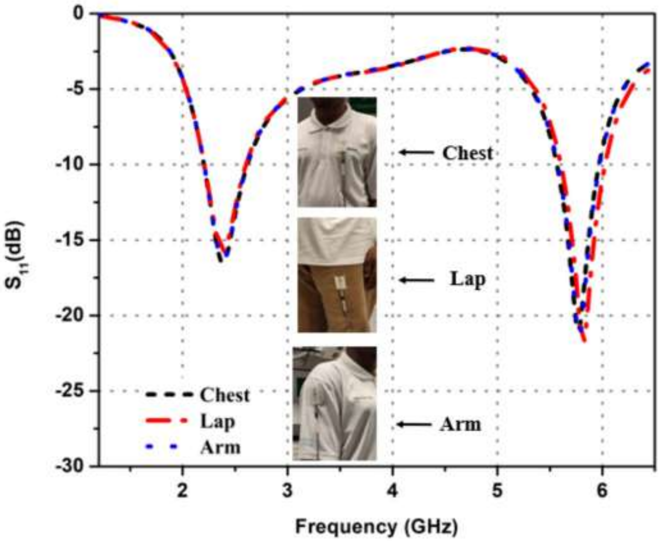

Fig. 26. Measured S_{11} for the antenna in various body settings: Chest, lap and arm.

S_{11} measurements were also conducted with the antenna placed on three body regions critical for biomedical applications: the chest (heart rate monitoring), arm (wearable device integration), and lap (mobility-focused sensing), as demonstrated in Fig. 25. These positions were selected to represent common deployment sites for health-monitoring systems, balancing anatomical relevance and functional use cases.

Figure 26 displays the measured S_{11} parameters, showing a minor frequency shift when the antenna is mounted on the lap. This deviation is attributed to the elevated dielectric constant of human tissues, which slightly shifts the upper resonant frequency due to increased electromagnetic coupling with the body.

To further assess on-body compatibility, E-plane radiation patterns were simulated for the antenna positioned on the chest, lap, and lap. As illustrated in Fig. 27, the patterns at 2.4 GHz and 5.8 GHz display negligible deviations across these placements, confirming minimal impact on radiation efficiency. Figure 28 quantifies the simulated gain variations: at 2.4 GHz as seen in Fig. 28a, gains span 3.8 to 4.6 dBi, while at 5.8 GHz as seen in Fig. 28b, gains range from 4.0 to 4.9 dBi. These results demonstrate the antenna's stability in diverse on-body scenarios, with performance fluctuations well within functional limits. Such consistency ensures reliable operation in wearable systems, where signal integrity is critical for real-world biomedical and mobility applications.

Table 6 presents the frequency shifts for different antenna placements (chest, lap, and arm) across the 2.4 GHz and 5.8 GHz bands. Since the variations in frequency are minimal compared to free space, they remain within the acceptable range for each band, indicating that the antenna design is effective even with body placement interference.

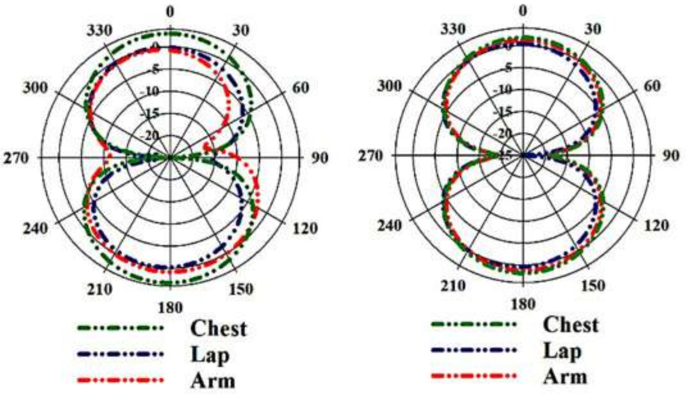

(a) (b)

Fig. 27. Radiation pattern, *E*-plane (φ = 0°) as a function of θ of the antenna at different body locations: (**a**) 2.4 GHz (**b**) 5.8 GHz.

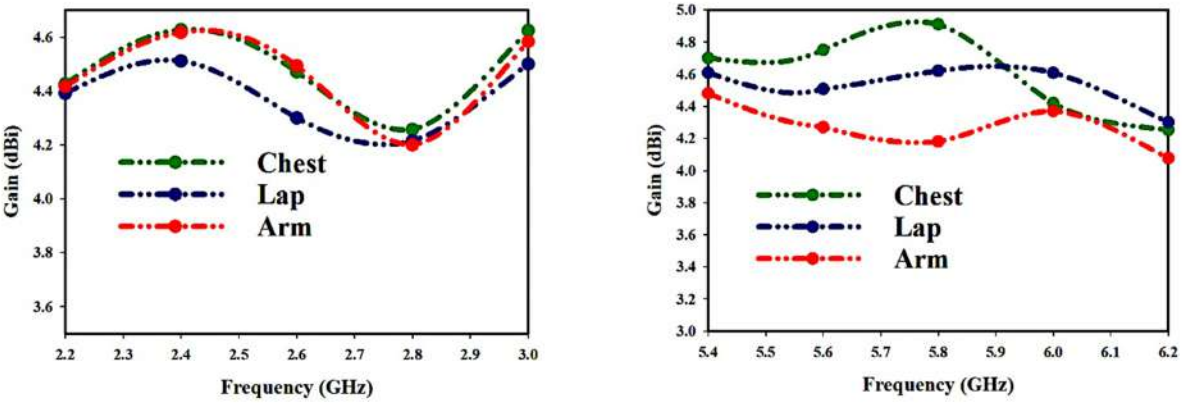

(a) (b)

Fig. 28. Gain variation of the antenna on various parts of human body (**a**) 2.4 GHz (**b**) 5.8 GHz.

Frequency Band	Free-Space	Chest	Lap	Arm
2.4 GHz				
Lower Frequency	2.382 GHz	2.371 GHz	2.369 GHz	2.380 GHz
Upper Frequency	2.511 GHz	2.510 GHz	2.506 GHz	2.509 GHz
Δf (Lower)	-	-0.011 GHz	-0.013 GHz	+ 0.002 GHz
Δf (Upper)	-	+ 0.001 GHz	-0.005 GHz	-0.002 GHz
5.8 GHz				
Lower Frequency	5.634 GHz	5.621 GHz	5.719 GHz	5.629 GHz
Upper Frequency	5.911 GHz	5.909 GHz	5.931 GHz	5.918 GHz
Δf (Lower)	-	+ 0.013 GHz	+ 0.085 GHz	-0.005 GHz
Δf (Upper)	-	-0.002 GHz	+ 0.020 GHz	+ 0.007 GHz

Table 6. Frequency shifts for antenna placement configurations (Free space, Chest, Lap, Arm) in 2.4 GHz and 5.8 GHz band.

Layer	Bone	Muscle	Fat	Skin
Permittivity (F/m)	18.49	48.49	4.90	35.93
Density (kg/m^2)	1008	1040	910	1100
Conductivity (Ωm)	0.82	4.96	0.15	3.72
Thickness (mm)	13	20	5	2

Table 7. Characteristics of human body tissue[56].

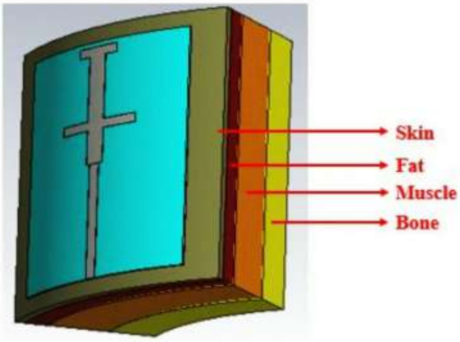

Fig. 29. Anatomical approximation of layered human tissues used for SAR simulations.

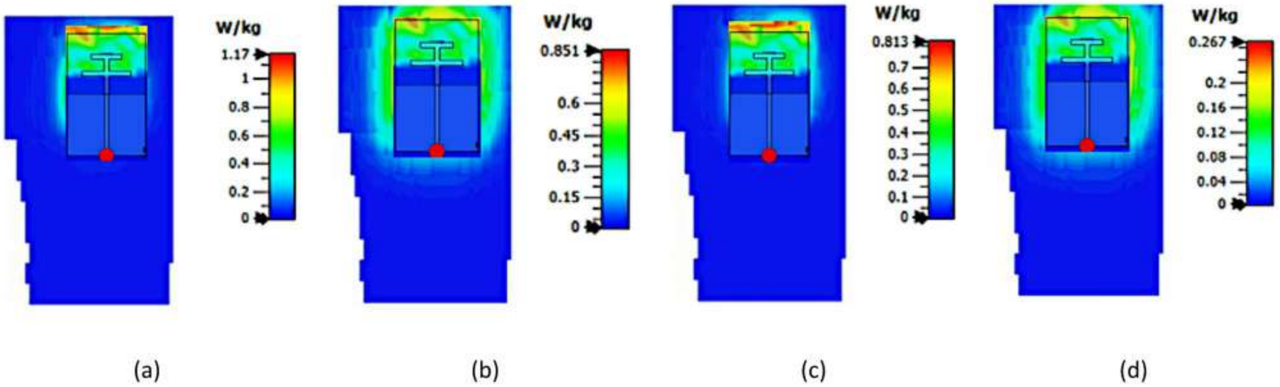

Fig. 30. Computed SAR distributions for the antenna at: (**a**) 2.4 GHz in 1-gram tissue, (**b**) 2.4 GHz in 10-gram tissue, (**c**) 5.8 GHz in 1-gram tissue, and (**d**) 5.8 GHz in 10-gram tissue.

SAR analysis

Growing concerns about the potential health effects of electromagnetic exposure, along with international safety regulations, have encouraged researchers to investigate how much electromagnetic energy is taken up by the human body during extended use. In the context of wearable antennas used in close proximity to the body, this involves analyzing the Specific Absorption Rate (SAR), which quantifies the electromagnetic energy absorbed by biological tissues per unit of body mass, as a critical safety metric. Following IEEE C95.1 guidelines, SAR levels were modeled using CST MWS software. The antenna's SAR characteristics were examined through simulations based on a layered human phantom model (composed of skin, fat, muscle, and bone) to reflect real-world tissue behavior. The phantom-to-antenna spacing was maintained at a standard distance of 2 cm in the simulation setup. The feed power was normalized to 100 mW for all SAR measurements. The voxel resolution used for simulations was 1 mm^3, and the dielectric properties were sourced from standard human tissue models as defined by the IEEE C95.1 guidelines, with specific values for bone, muscle, fat, and skin layers, as detailed in Table 7. Averaging mass definitions for SAR measurements were set to the standard 1 g and 10 g tissue averages, which are commonly used in health-related regulatory standards. Figure 29 illustrates the simplified anatomical representation created to emulate realistic tissue responses. This model supports accurate simulations of energy absorption for wearable antenna use cases. Figure 30 presents SAR measurements corresponding to both 1 g and 10 g of tissue at the antenna's intended operating frequencies. At 2.4 GHz as illustrated in Figs. 30a, b, SAR

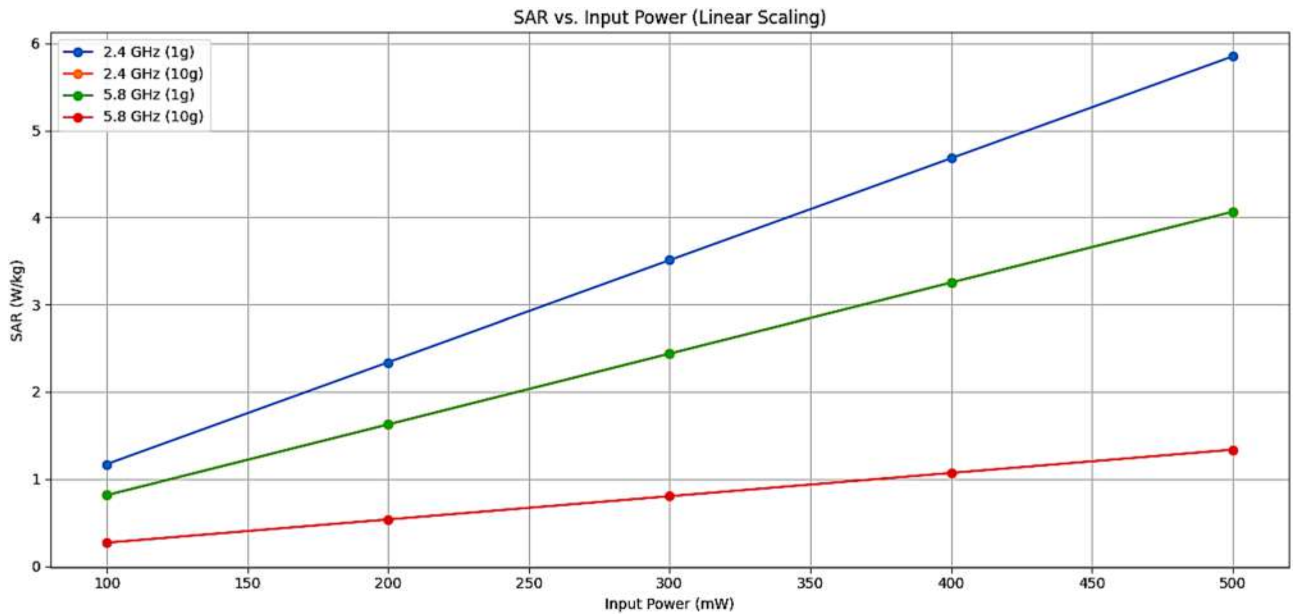

Fig. 31. SAR vs. input power characteristics of the antenna for both 2.4 GHz and 5.8 GHz frequencies bands.

Ref.	Frequency (GHz)	Bandwidth (%)	Substrate	Substrate Thickness (mm)	Efficiency (%)	Gain (dBi)	AMC used?	SAR (W/kg)	ML Prediction	Dimensions (mm^2) λ_0 @ 2.4 GHZ
8	2.4/5.8	3.8/5.2	Rogers	1.52	91.4/92.3	3.74/5.13	No	0.57/0.13	No	$0.33\lambda_0 \times 0. 35\lambda_0$
36	2.4/5.8	2.57/5.22	Felt	1	NA	1.9/5.9	No	0.25/0.074	No	$0.8\lambda_0 \times 0.8\lambda_0$
57	2.4/5.8	4.2/10.5	FR-4	0.6	NA	1.2/7.9	No	1.26/0.46	No	$0.4\lambda_0 \times 0.4\lambda_0$
58	2.4/5.8	4.9/3.8	Felt	2	70.1/72.5	6.33/6.02	No	0.042/0.09	No	$0.8\lambda_0 \times 0.8\lambda_0$
59	2.4/5.8	NA	Denim	Superstrate/Substrate 1.25/3.75	16/25	1.69/4.12	No	1.67/1.12	No	$0.4\lambda_0 \times 0.4\lambda_0$
60	2.4/5.8	6/3.6	Rogers	1.575	90/84	1.1 / 4.5	No	NA	No	$0.64\lambda_0 \times 0.64\lambda_0$
61	2.4/3.5	2.04/3.44	FR-4	1.6	80/80	5.06/6.33	No	0.19/1.18	No	$0.32\lambda_0 \times 0.24\lambda_0$
62	2.4/5.8	3.75/3.97	Thick Felt	1.574	71.9/92.5	1.75 / 5.69	No	1.63/1.56	No	$0.36\lambda_0 \times 0.36\lambda_0$
This work	2.4/5.8	9.7/7.8	Rogers	0.5	91/93	4.0/6.2	No	0.851/0.267	Yes	$0.24\lambda_0 \times 0.39\lambda_0$

Table 8. Performance comparison with existing literature. Note: NA – Not available.

measurements were 1.17 W/kg (1 g) and 0.851 W/kg (10 g) with an input power of 100 mW. At 5.8 GHz as shown in Figs. 30c, d, SAR values were 0.813 W/kg (1 g) and 0.267 W/kg (10 g). These values meet the FCC and ICNIRP safety criteria (1.6 W/kg for 1 g and 2.0 W/kg for 10 g), demonstrating that the antenna satisfies international safety standards for wearable health-related devices.

The SAR vs. input power characteristics for both 2.4 GHz and 5.8 GHz frequencies across 1 g and 10 g tissue is presented in Fig. 31. It confirms the expected linear scaling of SAR with input power. This cross-check plot ensures the consistency of SAR scaling with varying input power, which is a key aspect of SAR testing for wearable devices.

Table 8 presents a comparative analysis of the dual-band body-mounted antenna developed in this work with previously reported designs. The analysis is based on critical parameters such as operating frequency, substrate material, SAR values, efficiency, gain, and ML optimization framework. The proposed antenna achieves dual-band operation (2.4/5.8 GHz) within a compact $30 \times 48.8\ \text{mm}^2$ dimensions, resolving the trade-off between miniaturization and performance. Notably, existing antennas in[36,57–60] exhibit larger dimensions than the proposed design. Unlike rigid counterparts[57,61], the proposed antenna maintains stable reflection coefficients (< -10 dB) under bending (30 mm, 60 mm and 90 mm radii). Furthermore, SAR validation confirms compliance with FCC/ICNIRP safety limits (0.57–0.98 W/kg), addressing a critical oversight in prior works[60].

Conclusion

This study demonstrates a miniaturized dual-frequency wearable antenna for WBAN, optimized using machine learning (ML) to enhance performance, safety, and computational efficiency. Fabricated on a 30 × 48.8 mm² Rogers Duroid 3003™ substrate, the antenna achieves dual-band operation at 2.4 GHz (9.7% bandwidth, 4.0 dBi gain, 91% efficiency) and 5.8 GHz (7.8% bandwidth, 6.2 dBi gain, 93% efficiency), with stable radiation patterns—bidirectional in the E-plane and omnidirectional in the H-plane. SAR validation confirms compliance with FCC/ICNIRP safety standards, yielding values of 1.17 W/kg (1 g tissue) and 0.851 W/kg (10 g tissue) at 2.4 GHz, and 0.813 W/kg (1 g) and 0.267 W/kg (10 g) at 5.8 GHz. Bending tests to simulate the real-world deployment of the antenna on (arm, chest, and lap) validate mechanical robustness, maintaining reflection coefficients below − 10 dB across bending radii of 30–90 mm. The design's S_{11} was efficiently predicted using a random forest ML framework, achieving 87.70% accuracy (R^2) with minimal prediction errors (MAE: 0.35, MSE: 0.89, MSLE: 0.21, RMSLE: 0.35, RMSE: 0.94). By integrating ML-driven optimization with compact, flexible design, this work addresses critical challenges in WBANs balancing safety, miniaturization, and computational efficiency while advancing the practical deployment of wearable antennas in WBAN applications. While this study focused on the antenna's performance under standard conditions, we acknowledge that environmental factors such as rain, humidity, and temperature can significantly affect the performance of wearable antennas in real-world WBAN applications. These factors can cause variations in the antenna's resonant frequency, impedance matching, and overall efficiency. Future studies will incorporate these environmental conditions into the optimization process to better simulate the dynamic nature of WBAN deployment and ensure the antenna's robust performance across diverse scenarios. This will be crucial for ensuring the reliability and safety of wearable antenna systems in practical, on-body environments.

Data availability

The datasets used and/or analysed during the current study available from the corresponding author on reasonable request.

Received: 6 August 2025; Accepted: 3 November 2025

References

1. Abdelghany, M. A., Ahmed, M. I., Ibrahim, A. A., Desai, A. & Ahmed, M. F. Textile antenna with dual bands and SAR measurements for wearable communication, *Electronics* **13**, 12, 2251, (2024).
2. Al-Gburi, A. J. A. et al. Super compact UWB monopole antenna for small IoT devices. *Comput. Mater. Contin.* **73** (2), 2785–2799. https://doi.org/10.32604/cmc.2022.028074 (2022).
3. Preethichandra, D., Piyathilaka, L., Izhar, U., Samarasinghe, R. & De Silva, L. C. Wireless body area networks and their applications—A review. *IEEE Access.* **11**, 9202–9220 (2023).
4. Kaleem, M. & Devarajan, G. G. Energy-efficient classification strategy for detecting interference and malicious sensor nodes in wireless body area networks. *Cyber Secur. Appl.* **2**, 100048 (2024).
5. Sid, A., Cresson, P. Y., Joly, N., Braud, F. & Lasri, T. A flexible and wearable dual band bio-based antenna for WBAN applications. *AEU. Int. J. Electron. Commun.* **157**, 154412 (2022).
6. Ashyap, A., Raad, R., Tubbal, F., Khan, W. & Abulgasem, S. Comprehensive review of wearable antennas with flexible periodic structures for Body-Effect mitigation. *IEEE Access*, (2025).
7. Ali, U., Ullah, S., Kamal, B., Matekovits, L. & Altaf, A. Design, analysis and applications of wearable antennas: A review. *IEEE Access.* **11**, 14458–14486 (2023).
8. Musa, U. et al. Design and analysis of a compact dual-band wearable antenna for WBAN applications. *IEEE Access.* **11**, 30996–31009 (2023).
9. Islam, M. S., Azam, S. K., Hossain, A. Z., Ibrahimy, M. I. & Motakabber, S. A low-profile flexible planar monopole antenna for biomedical applications. *Eng. Sci. Technol. Int. J.* **35**, 101112 (2022).
10. Kaur, N., Sivia, J. S. & Kumar, M. A design of planar monopole antenna for wireless applications. *Wireless Pers. Commun.* **125** (3), 2201–2218 (2022).
11. Zarifi, D. & Aslinezhad, M. Design of an extremely wideband planar dipole antenna for Sub-3 ghz applications. *AEU. Int. J. Electron. Commun.* **195**, 155774 (2025).
12. Ullah, S., Marasco, I., D'Orazio, A. & Magno, G. Graphene-based programmable dual dipole antenna with parasitic elements. *Opt. Quant. Electron.* **57** (2), 1–16 (2025).
13. Abd-Elsalam, R. W., Seleem, H. E., Abd-Elnaby, M. M. & Hussein, A. H. Low SAR compact wideband/dual-band semicircular slot antenna structures for sub-6 GHz 5G wireless applications, *EURASIP J. Wireless Commun. Netw.* **1**, 3, 2025. (2025).
14. Tamma, M., Boonjue, A., Ramphueiphad, S. & Kampeephat, S. Performance improvement of slot antenna with metamaterial for modern wireless communication. *Res. Eng.* **23**, 102686 (2024).
15. Patel, K. & Behera, S. K. Design of band reconfigurable Koch fractal antenna for wideband applications. *AEU Int. J. Electron. Commun.* **188**, 155592 (2025).
16. Attioui, S., Khabba, A., Aguni, L., Ibnyaich, S. & Zeroual, A. Hybrid fractal antenna design for UWB applications inspired by Giuseppe Peano and Sierpinski carpet. *Analog Integr. Circuits Signal Process.* **122** (3), 29 (2025).
17. Pravesh, S., Nandana, M., Akshaya, R. & Christina Josephine Malathi, A. Study and design of heart-shaped microstrip patch antenna for SART applications. *Res. Eng.* **25**, 103819 (2025).
18. Zhu, J. & Liu, J. Design of microstrip antenna integrating 24 GHz and 77 GHz compact high-gain arrays, *Sensors* **25**, 2, 481, (2025).
19. Yu, Z. et al. A flexible multiband dendritic structure fractal antenna for 4G/5G/WLAN/Bluetooth applications, *Int. J. RF Microwave Computer Aided Eng.* **1**. 6496757, (2023).
20. Bouazizi, A. et al. A dual-band case-printed planar inverted-F antenna design with independent resonance control for wearable short range telemetric systems. *Int. J. RF Microw. Comput. Aided Eng.* **29** (8), e21781 (2019).
21. Mohan, C. & Florence, S. E. Miniaturised triangular microstrip antenna with metamaterial for wireless sensor node applications. *IETE J. Res.* **68** (2), 1177–1182 (2022).
22. Li, Y., Lu, Z. & Yang, L. CPW-fed slot antenna for medical wearable applications. *IEEE Access.* **7**, 42107–42112 (2019).
23. Shehbaz, M., Du, C., Zhou, D., Xia, S. & Xu, Z. Recent progress in dielectric resonator antenna: Materials, designs, fabrications, and their performance. *Appl. Phys. Rev.*, **10**, 2, (2023).

24. Sun, Y. X., Wu, D., Fang, X. S. & Yang, N. Compact quarter-mode substrate-integrated waveguide dual-frequency millimeter-wave antenna array for 5G applications. *IEEE Antennas. Wirel. Propag. Lett.* **19** (8), 1405–1409 (2020).
25. Aziz, A., Farhan, M., Sharif, A., Ijaz, U. & Safdar, N. A novel high permittivity ceramic-silicone composite substrate-based antenna for energy harvesting. *AEu. Int. J. Electron. Commun.* **184**, 155427 (2024).
26. Zheng, W., Li, H. & Liu, G. Design of circularly polarized smartwatch antenna with reactive loads. *IEEE Antennas. Wirel. Propag. Lett.* **22** (7), 1602–1606 (2023).
27. Purbey, D. P., Ghosal, S. & De, A. Shorting pin inspired coupling reduction in Dual-Band Dual-Polarized STAR antenna. *IEEE Antennas Wirel. Propag. Letters*, (2024).
28. Dam, T. H., Le, M. T., Nguyen, Q. C. & Nguyen, T. T. Dual-band metamaterial-based EBG antenna for wearable wireless devices, *Int. J. RF Microwave Computer Aided Engi*, **1**, 2232674, 2023. (2023).
29. Panda, S., Gupta, A. & Acharya, B. Wearable microstrip patch antennas with different flexible substrates for health monitoring system, *Materials Today: Proceedings*. **45**, 4002–4007, (2021).
30. Dey, A. B., Pattanayak, S. S., Mitra, D. & Arif, W. Investigation and design of enhanced decoupled UWB MIMO antenna for wearable applications. *Microw. Opt. Technol. Lett.* **63** (3), 845–861 (2021).
31. Dey, A. B., Kumar, S., Arif, W. & Anguera, J. Elastomeric textile substrates to design a compact, low-profile AMC-based antenna for medical and IoT applications. *IEEE Internet Things J.* **10** (6), 4952–4969 (2022).
32. Dey, A. B., Mitra, D. & Arif, W. Design of CPW fed multiband antenna for wearable wireless body area network applications. *Int. J. RF Microwave Comput. Aided Eng.* **30** (12), e22459 (2020).
33. Dey, A. B. & Arif, W. Design and analysis of a CPW-fed flexible ultrawideband antenna for microwave imaging of breast cancer. *Int. J. RF Microw. Comput. Aided Eng.* **32** (9), e23262 (2022).
34. Dey, A. B., Bhatt, U. & Arif, W. Design of a compact wearable ultrawideband Mimo antenna with improved portisolation. *Turkish J. Electr. Eng. Comput. Sci.* **29** (2), 897–912 (2021).
35. Dey, A. B. & Arif, W. On-body low-profile compact AMC-integrated wideband antenna for body area network applications. *IETE Tech. Rev.* **41** (2), 133–146 (2024).
36. Zhou, L., Fang, S. J. & Jia, X. A compact dual-band and dual-polarized antenna integrated into textile for WBAN dual-mode applications. *Progress Electromagnet. Res. Lett.* **91**, 153–161 (2020).
37. Li, H., Du, J., Yang, X. X. & Gao, S. Low-profile all-textile multiband microstrip circular patch antenna for WBAN applications. *IEEE Antennas. Wirel. Propag. Lett.* **21** (4), 779–783 (2022).
38. Musa, U. et al. Recent advancement of wearable reconfigurable antenna technologies: A review. *IEEE Access.* **10**, 121831–121863 (2022).
39. Al-Gburi, A. J. A. Coin-Sized Dual-Band Millimeter-Wave (mmWave) Antenna with Machine-Learning-Guided Impedance Prediction. *Progress In Electromagnetics Research M*. **136**, 1–12. https://doi.org/10.2528/PIERM25071303 (2025).
40. Dutta, K., Akinsolu, M. O., Mishra, P. K., Liu, B. & Guha, D. Application of machine learning-assisted global optimization for improvement in design and performance of open resonant cavity antenna. *IEEE Open. J. Antennas Propag.* **5** (3), 693–704 (2024).
41. El Misilmani, H. M. & Naous, T. Machine learning in antenna design: An overview on machine learning concept and algorithms, In: *International Conference on High Performance Computing & Simulation (HPCS)*, (IEEE, 2019).
42. Haque, M. A. et al. Regression supervised model techniques THz MIMO antenna for 6G wireless communication and IoT application with isolation prediction. *Res. Eng.* **24**, 103507 (2024).
43. Musa, U. et al. Machine learning-optimized dual-band wearable antenna for real-time remote patient monitoring in biomedical IoT systems. *Sci. Rep.* **15** (1), 30943 (2025).
44. Waly, M. I. et al. Optimization of a compact wearable LoRa patch antenna for vital sign monitoring in WBAN medical applications using machine learning. *IEEE Access.* **12**, 103860–103879 (2024).
45. Yahya, M. S. et al. Machine learning-optimized compact frequency reconfigurable antenna with RSSI enhancement for long-range applications. *IEEE Access.* **12**, 10970–10987 (2024).
46. Raza, M. U., Ren, H. & Yan, S. Dual-band monopole MIMO antenna array for UAV communication systems, *Sensors*, **24**,18, 5913, (2024).
47. Koziel, S. & Pietrenko-Dabrowska, A. Reduced-cost electromagnetic-driven optimisation of antenna structures by means oftrust-region gradient-search with sparse Jacobian updates. *IET Microwaves Antennas Propag.* **13** (10), 1646–1652 (2019).
48. Devisasi Kala, D. & Sundari, D. T. A review on optimization of antenna array by evolutionary optimization techniques. *Int. J. Intell. Unmanned Syst.* **11** (1), 151–165 (2023).
49. Yahya, M. S., Soeung, S., Rahim, S. K. A., Geok, T. K. & Musa, U. Machine learning-optimized wearable antenna for LoRa localization. *IEEE Access*, (2024).
50. Yahya, M. S. et al. LoRa microstrip patch antenna: a comprehensive review. *Alexandria Eng. J.* **103**, 197–221 (2024).
51. Musa, U. et al. Investigation of the nonlinearity of PIN diode on frequency reconfigurable patch antenna, *J. Eng.*. **9** e12308, (2023).
52. Odiamenhi, M. et al. Advancements and challenges in antenna design and rectifying circuits for radio frequency energy harvesting, *Sensors* **24**, 21, 6804, (2024).
53. Yahya, M. S. et al. Triple-band reconfigurable monopole antenna for long-range IoT applications, *Sensors*. **23**, 12, 5359, (2023).
54. Yahya, M. S. et al. A compact Dual-Band antenna for enhanced Vehicle-to-Vehicle communication. *Transp. Res. Procedia*. **84**, 370–377 (2025).
55. Waly, M. I. et al. Advancement of a high-efficiency wearable antenna enabling wireless body area networks. *IEEE Access.* **11**, 138325–138335 (2023).
56. El Atrash, M., Abdalla, M. A. & Elhennawy, H. M. Gain enhancement of a compact thin flexible reflector-based asymmetric meander line antenna with low SAR. *IET Microwaves Antennas Propag.* **13** (6), 827–832 (2019).
57. Zhao, C. & Geyi, W. Design of a dual band dual mode antenna for on/off body communications. *Microw. Opt. Technol. Lett.* **62** (1), 514–520 (2020).
58. Zhou, L., Fang, S. & Jia, X. Dual-band and dual-polarised circular patch textile antenna for on-/off-body WBAN applications. *IET Microwaves Antennas Propag.* **14** (7), 643–648 (2020).
59. Bhattacharjee, S., Maity, S., Chaudhuri, S. R. B. & Mitra, M. A compact dual-band dual-polarized omnidirectional antenna for on-body applications. *IEEE Trans. Antennas Propag.* **67** (8), 5044–5053 (2019).
60. Xiaomu, H., Yan, S. & Vandenbosch, G. A. Wearable button antenna for dual-band WLAN applications with combined on and off-body radiation patterns. *IEEE Trans. Antennas Propag.* **65** (3), 1384–1387 (2017).
61. Ahmad, S., Ghaffar, A., Hussain, N. & Kim, N. Compact dual-band antenna with paired L-shape slots for on-and off-body wireless communication, *Sensors*, **21**, 23, 7953, (2021).
62. Ali, S. M. et al. Design and evaluation of a button sensor antenna for on-body monitoring activity in healthcare applications, *Micromachines* **13**, 3,475, (2022).

Acknowledgements

The authors sincerely thank Universiti Teknologi PETRONAS and Universiti Teknikal Malaysia Melaka for their generous support in funding this research.

Author contributions

M. S. Yahya contributed to conceptualization, investigation, data curation, visualization, and writing – original draft. U. Musa and M. S. Zidan handled methodology, software, data analysis, visualization, and writing – review & editing. S. Soeung and Z. Zakaria undertook investigation and writing – review & editing. L. Iznita Izhar contributed to methodology, investigation, and writing – review & editing. Ahmed J. A. Al-Gburi provided supervision, project administration, resources, funding acquisition, methodology, and writing – review & editing. All authors approved the final manuscript.

Funding

The authors express their gratitude to Universiti Teknikal Malaysia Melaka (UTeM) and the Ministry of Higher Education (MOHE) of Malaysia for their valuable support in funding and facilitating this project.

Declarations

Competing interests

The authors declare no competing interests.

Ethical approval and consent to participate

All methods were carried out in accordance with relevant guidelines and regulations. The experimental protocol involving human participants was reviewed and approved by the Universiti Teknologi PETRONAS (UTP) Human Research Ethics Committee. Informed consent was obtained from all subjects prior to participation in the study.

Additional information

Correspondence and requests for materials should be addressed to A.J.A.A.-G.